Int J Earth Sci (Geol Rundsch) (2017) 106:875–897
DOI 10.1007/s00531-016-1339-7

ORIGINAL PAPER

Zircon U–Pb ages, Hf isotope data, and tectonic implications of Early–Middle Triassic granitoids in the Ailaoshan high-grade metamorphic belt of Southeast Tibet

Wenbin Wu[1] · Junlai Liu[1] · Xiaoyu Chen[1] · Lisheng Zhang[1]

Received: 6 January 2016 / Accepted: 7 May 2016 / Published online: 31 May 2016

Abstract The Ailaoshan tectonic belt, where the effects of the Paleo-Tethyan ocean evolution and Indian–Eurasian plate collision are superimposed, is one of the most significant geological discontinuities in western Yunnan province of southeast Tibet. An Ailaoshan micro-block within the belt is bounded by the Ailaoshan suture zone to the west and the Red River Fault to the east, and consists of low- and high-grade metamorphic belts. Late Permian–Middle Triassic granitoids that are widely distributed to the west of the Ailaoshan suture zone and within the Ailaoshan micro-block may yield significant information on the Tethyan tectonic evolution of the Ailaoshan tectonic belt. This study reports new LA–ICP–MS zircon U–Pb geochronology and Hf isotope data of four granitoids from the Ailaoshan high-grade metamorphic belt. Zircon grains from the Yinjie granitoid do not have inherited cores and yield a weighted mean U–Pb age of 247.1 ± 2.0 Ma. The zircon $\varepsilon_{Hf}(t)$ values range from 7.8 to 12.1, and Hf model ages from 775 to 546 Ma, indicating that the granitoid was derived from juvenile crust. The rims of zircons from the Majie and Yuanjiang granitoids yield weighted mean U–Pb ages of 239.5 ± 1.8 and 237.9 ± 2.6 Ma, respectively, whereas the cores yield ages of 1608–352 Ma. The $\varepsilon_{Hf}(t)$ values of zircon rims range from −20.4 to −5.3, yielding Hf model ages from 2557 to 1606 Ma and suggesting that the source magma of the Majie and Yuanjiang granitoids was derived from ancient crust. An additional granitoid located near the Majie Village yields a zircon U–Pb age of 241.2 ± 1.0 Ma. Based on our geochronological and geochemical data, combined with geological observations, we propose that the Ailaoshan micro-block was derived from the western margin of the Yangtze block, and is comparable to the Zhongzan and Nam Co micro-blocks. The presence of late Permian mafic rocks with rift-related geochemical characteristics within the Ailaoshan micro-block, together with granitoids derived from partial melting of ancient/juvenile crust, indicates the presence of an Ailaoshan rift. This possible rift may correspond to the Ganzi–Litang Ocean to the northwest and the Jinping–Song Da rift to the southeast. It is suggested that westward subduction of the Jinshajiang–Ailaoshan–Song Ma oceanic lithosphere triggered the separation of the Zhongzan, Ailaoshan, and Nam Co micro-blocks from the western passive continental margin of the Yangtze block through the opening of the Ganzi–Litang–Ailaoshan–Jinping–Song Da ocean/rift. This ocean/rift may represent a subsidiary branch of the Paleo-Tethyan Ocean along the western margin of the Yangtze block.

Keywords Paleo-Tethys · Western margin of the Yangtze block · Ailaoshan tectonic belt · Granitoid · Zircon U–Pb age and Hf isotope · Ailaoshan rift

Introduction

The Tethyan orogenic belt exemplifies the dynamics of plate tectonics during the classical Wilson cycle. The Tethyan belt in Southeast Asia comprises a collage of micro-continental blocks and suture zones. The tectonic evolution of the belt involved a sequence of processes that record the opening and closure of the Tethyan Ocean. The successive separation and northward translation of the eastern Qiangtang–Simao–Indochina, western Qiangtang–Sibumasu, and

✉ Junlai Liu
jliu@cugb.edu.cn

[1] State Key Laboratory of Geological Processes and Mineral Resources, China University of Geosciences, Beijing 100083, China

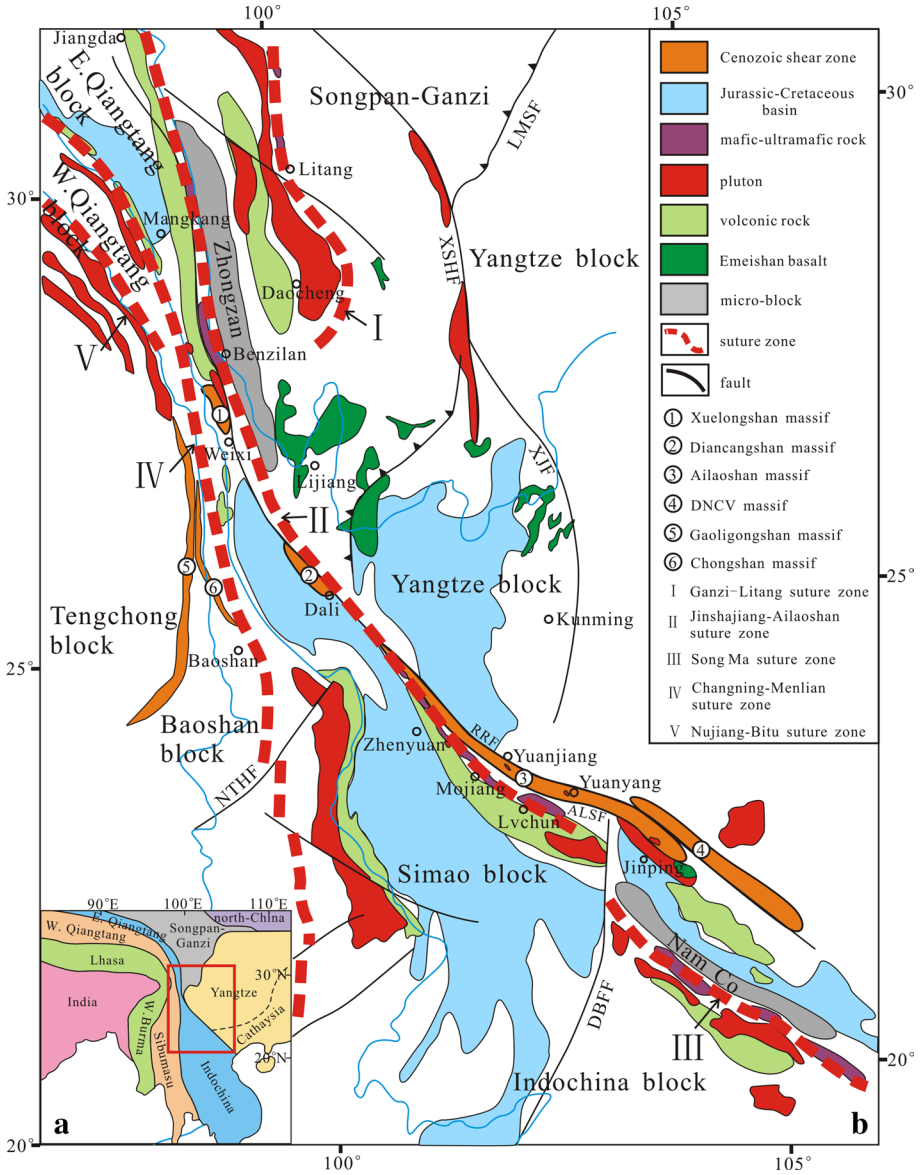

Fig. 1 **a** Distribution of principal continental blocks of Southeast Asia (modified after Deng et al. 2014); **b** simplified geological map of Sanjiang region (modified after Liu et al. 2012b; Zi et al. 2013; Deng et al. 2014). *ALSF* Ailaoshan fault, *DBFF* Dien Bien Phu fault, *LMSF* Longmenshan fault, *NTHF* Nantinghe fault, *RRF* Red River fault, *XSHF* Xianshuihe fault, *XJF* Xiaojiang fault

Lhasa–Western Burma blocks from the northeastern margin of the Gondwana continent contributed to the opening of the Paleo-, Meso-, and Neo-Tethyan Ocean, respectively (Metcalfe 2006, 2013; Deng et al. 2014). The subduction of the Tethyan oceanic plates and the collisions and accretions of these micro-continental blocks to the southern margin of the Eurasian Plate resulted in the formation of several suture zones and magmatic arcs (Fig. 1).

Remnants of the main Eastern Tethyan Ocean crust are preserved within the Longmuco–Shuanghu, Changning–Menglian, Chiang Mai/Inthanon, and Bentong–Raub suture zones. Located between the eastern Qiangtang–Simao–Indochina block and the Yangtze block, the Ailaoshan suture zone is interpreted to link the Jingshajiang suture zone to the northwest and the Song Ma suture zone to the southeast (Fig. 1). The suture zones represent a subsidiary branch (Zhong 1998; Metcalfe 2006, 2013; Jian et al. 2009a, b; Hu et al. 2015) or a back-arc ocean basin (Metcalfe 2006, 2013; Fan et al. 2010) of the main eastern Tethyan Ocean. Several studies have proposed that the initial opening of the Jinshajiang–Ailaoshan–Song Ma Ocean began in the Silurian (Jian et al. 2009b; Xia et al. 2015) and that oceanic spreading continued from the Late Devonian to the early Permian (Wang et al. 2000; Jian et al. 2008, 2009a, b; Zi et al. 2012a; Vuong et al. 2013; Lai et al. 2014b). Based on the existence of a volcano-plutonic arc along the eastern margin of the eastern Qiangtang–Simao–Indochina block, it is commonly interpreted that the oceanic lithosphere underwent westward subduction from the middle Permian to the Early Triassic (Jian et al. 2009a, b; Fan et al. 2010; Liu et al. 2011; Zi et al. 2012b; Lai et al. 2014a). Subsequently, the collision of the eastern

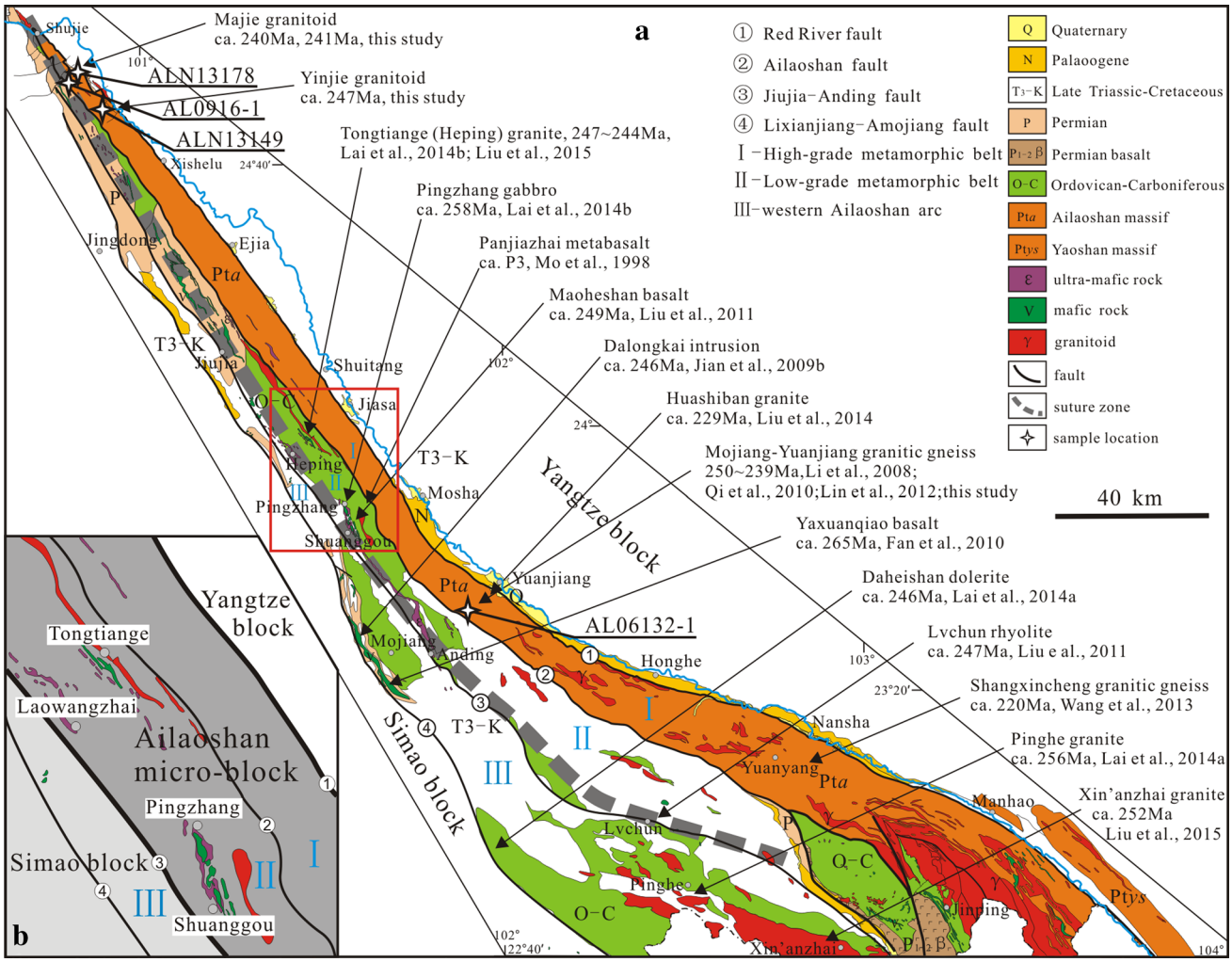

Fig. 2 **a** Geological map of the Ailaoshan tectonic belt showing the distribution of Permo-Trassic magmatism and the sample locations, the ages are from Mo et al. (1998), Jian et al. (2009b), Qi et al. (2010), Liu et al. (2011, 2014, 2015a), Li et al. (2008), Lin et al. (2012), Lai et al. (2014a, b), and this study; **b** schematic geological map of Laowangzhai-Shuanggou area, showing the major tectonic units

Qiangtang–Simao–Indochina and Yangtze blocks resulted in collision-related magmatism, metamorphism, and deformation (Zhu et al. 2011; Liu et al. 2012b, 2014, 2015a; Zi et al. 2012c, 2013; Lai et al. 2014a). All the geological units are unconformably overlain by the Late Triassic molasse sequences, marking the final closure of the main Paleo-Tethyan Ocean (Zhong 1998; Wang et al. 2000).

The Tertiary Ailaoshan–Red River (ASRR) shear zone comprises the Xuelongshan, Diancangshan, Ailaoshan, and Day Nui Con Voi metamorphic cores, and is a left-lateral strike-slip shear zone that extends for more than 1000 km from Southeast Tibet to the South China Sea (Fig. 1b). The shear zone, represented by the Ailaoshan high-grade metamorphic belt in the Ailaoshan area, plays an important role in accommodating the southeastward extrusion and rotation of the Indochina block as a result of Indian–Eurasian plate collision and post-collisional processes (Tapponnier et al. 1982, 1990; Leloup et al. 1995; Searle 2006; Cao et al. 2011a; Liu et al. 2012a), and it may have caused a marked transformation and destruction of the Ailaoshan suture zone (Figs. 1b, 2).

The Jinshajiang and Song Ma tectonic belts are located along the northern and southern extensions of the Ailaoshan tectonic belt, respectively, and they possess marked similarities in the spatial distribution of various features. From west to east, the former consists of the Jomda–Weixi volcanic belt, the Jinshajiang suture zone, the Zhongzan block, the Yidun arc, and the Ganzi–Litang suture zone. From west to east, the Song Ma tectonic belt consists of the Truong Son–Song Ca magmatic belt, the Song Ma suture zone, the Nam Co block, and the Song Da rift (Liu et al. 2012b). The Ailaoshan tectonic belt comprises, from west to east, a volcanic belt, a suture zone, a low-grade metamorphic belt, and a high-grade metamorphic belt (Fig. 2). In addition to controversy regarding the subduction polarity

of the Jinshajiang–Ailaoshan–Song Ma Ocean, the spatial–temporal evolutions of the Jinshajiang Ocean compared with the Ganzi–Litang Ocean, and of the Song Ma Ocean compared with the Song Da rift, are widely debated (Lepvrier et al. 2004; Reid et al. 2005; Roger et al. 2008, 2010; Liu et al. 2012b). The extensive volcanic and plutonic rocks to the west of the Ailaoshan suture zone are considered to be the products of the westward subduction of the Ailaoshan oceanic plate beneath the Simao block (Jian et al. 2008, 2009a, b; Fan et al. 2010; Liu et al. 2011, 2015a; Lai et al. 2014a). Some granitoids, although cropping out to the east of the Ailaoshan suture zone or even within the Ailaoshan high-grade metamorphic belt, have also been attributed to subduction/collision (Li et al. 2008; Qi et al. 2010; Lin et al. 2012; Lai et al. 2014b; Liu et al. 2014, 2015a).

To improve our understanding of the Tethyan evolution along the Ailaoshan tectonic belt, it is essential to determine whether the granitoids located to the east of the Ailaoshan suture zone formed in relation to the closure of the Ailaoshan Ocean or were generated by other processes. Additionally, the comparative evolutions of different micro-blocks and oceans/rifts along the Jinshajiang–Ailaoshan–Song Ma belt may have important implications for the dynamics of plate subduction along convergent boundaries. In this contribution, we report new LA–ICP–MS zircon U–Pb geochronology and Hf isotope data from granitoids within the Ailaoshan high-grade metamorphic belt. Our geochronological and geochemical data from granitoids along the Ailaoshan high-grade metamorphic belt support the existence of the Ailaoshan micro-block and the Ailaoshan rift. We show that the subduction of the Ailaoshan oceanic plate led to the separation of the Ailaoshan micro-block from the Yangtze block via the formation of an Ailaoshan rift between the Indochina and Yangtze blocks. The Ailaoshan rift is connected to the Gangzi–Litang Ocean to the northwest and the Jinping–Song Da rift to the southeast.

Geological setting

The Sanjiang–Indochina region in southeastern Tibet (Fig. 1), bounded by the Sagaing Fault to the west and the Red River Fault to the east, is a collage of Gondwana-derived micro-blocks. The convergence of these micro-blocks produced several ophiolite belts together with volcanic arcs and accretionary complexes from the Paleozoic to the Mesozoic.

In the Ailaoshan tectonic belt, several tectonic units are bounded or separated by the Lixianjiang–Amojiang, Jiujia–Anding, Ailaoshan, and Red River faults, including, from west to east, the Lanping–Simao block, the western Ailaoshan magmatic arc belt, the Ailaoshan suture zone, a low-grade metamorphic belt, a high-grade metamorphic belt, and the southwestern margin of the Yangtze block, respectively (Fig. 2). The high-grade metamorphic belt, which represents part of the ASRR shear zone, is the result of India–Eurasia collision. Given its distinctive tectonic evolution, especially in terms of Cenozoic deformation, metamorphism, and magmatism, the area bounded by the Ailaoshan suture zone to the west and the Red River Fault to the east is referred to here as the "Ailaoshan micro-block". This block consists of the low-grade and high-grade metamorphic belts described above (Fig. 2b).

The Ailaoshan high-grade metamorphic belt is composed mainly of garnet/sillimanite–biotite–plagioclase gneiss, biotite/two-mica schist, and augen/banded migmatite with less amphibolite, calc-silicate marble, and quartzite. These rocks range in age from Paleoproterozoic to early Paleozoic (Zhai et al. 1990; Qi et al. 2012; Wang et al. 2013c; Cai et al. 2014). The Paleo-Mesoproterozoic whole-rock Sm–Nd and Rb–Sr isochron ages of amphibolite have led to the suggestion that the high-grade metamorphic rocks are part of the Precambrian crystalline basement of the Yangtze block (Zhai et al. 1990). Recent studies have revealed that Neoproterozoic rocks are widespread, including the Daping plutonic rocks (Qi et al. 2012), the Yuanyang granitic gneisses (Wang et al. 2013c), and the Jinping and Yuanyang amphibolites (Cai et al. 2014). Detrital zircon grains from quartzite define several age populations ranging from Paleoproterozoic to Middle Cambrian (Wang et al. 2013c). These rocks were intruded by voluminous Permo–Triassic biotite/muscovite granitoids (Li et al. 2008; Qi et al. 2010; Lin et al. 2012; Liu et al. 2014). All the metamorphic and plutonic rocks were affected by intense left-lateral strike-slip shearing, forming mylonitic fabrics. These strongly sheared rocks usually exhibit steeply dipping foliations and subhorizontal lineations, which are both sub-parallel to the northwest-trending metamorphic belt (Fig. 3a). Pressure–temperature (P–T) data show that peak metamorphism occurred under amphibolite-facies conditions (3–7 kbar and 550–780 °C; Leloup et al. 1993, 1995). The age of sinistral shearing (Fig. 3b) is constrained by the emplacement ages of syn-kinematic leucogranites (31.9–24.2 Ma; Leloup et al. 1995; Searle et al. 2010; Tang et al. 2013; Liu et al. 2015b). There are also numerous small-scale mafic–ultramafic intrusions within the high-grade metamorphic belt (Figs. 2, 3d).

The Ailaoshan and Diancangshan high-grade metamorphic belts are lithologically similar to each other and have comparable deformation and metamorphic histories. The separation of the Ailaoshan and Diancangshan belts possibly resulted from sinistral dismemberment of the ASRR shear zone, followed by uplift and dextral offsetting along the Quaternary Red River Fault (Leloup et al. 1995).

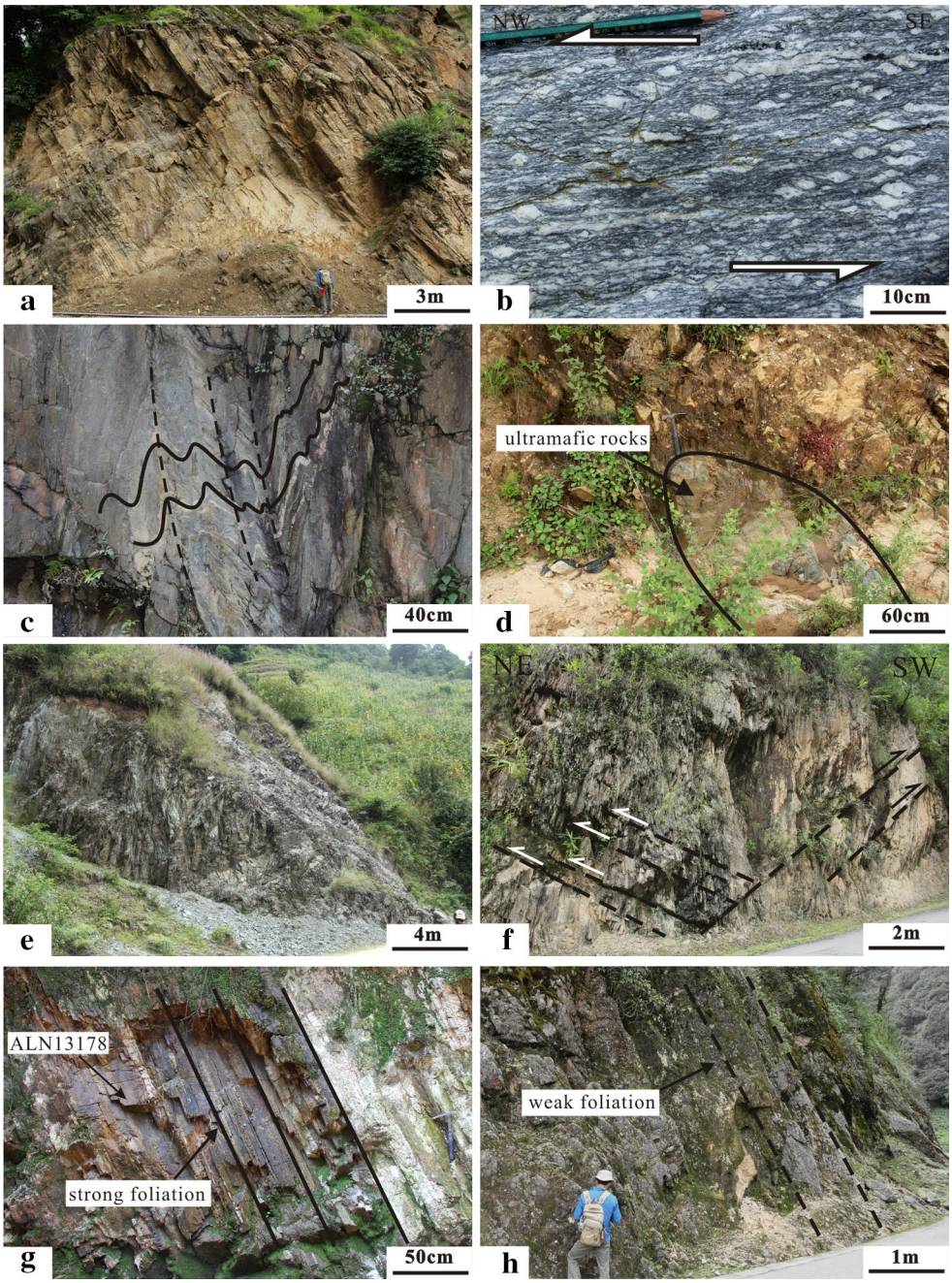

Fig. 3 Outcrops of major geological units and typical structural features in the Ailaoshan tectonic belt. **a** steeply dipping foliation in gneisses of the high-grade metamorphic belt; **b** sigma-shaped feldspar porphyroclasts indicating left-lateral shearing; **c** early penetrative foliations in phyllites and meta-siltstones of the low-grade metamorphic belt were folded with subvertical axial planar cleavages; **d** small-scale ultramafic intrusions within the high-grade metamorphic belt; **e** fragment of ophiolite suit; **f** steeply dipping axial cleavages and thrust faults in Late Triassic terrestrial rocks; **g** granitoids within the high-grade metamorphic belt were strongly mylonitized with pervasive foliations; **h** granitoids within the low-grade metamorphic belt were affected by the shearing, showing weak foliations

The Ailaoshan low-grade metamorphic belt lies to the southwest of the high-grade metamorphic belt, across the Ailaoshan Fault. It consists mainly of a sequence of greenschist-facies rocks that originated from Paleozoic shallow- to deep-marine carbonates, siliciclastic strata, and volcanic rocks. The volcano-sedimentary sequence is comparable to the Paleozoic passive continental margin sequence of the western Yangtze block. The dominant structural feature of the greenschist-facies rocks is their polystage deformation. The early penetrative foliations in biotite/two-mica schist, phyllite, and meta-siltstone were subsequently folded, resulting in subvertical axial planar cleavages (Fig. 3c). The

age of deformation and metamorphism is considered to be earlier than Late Triassic, as demonstrated by the unconformity between these rocks and overlying Late Triassic molasse.

The Early Devonian–late Carboniferous ophiolite suites occur within or along the southwestern margin of the low-grade metamorphic belt (Figs. 2, 3e). They consist of several fragments that are typically a few tens to hundreds of meters long. The fragments include meta-peridotite, diabase, basalt, plagiogranite, and radiolarian chert, representing remnants of the Ailaoshan Ocean (Zhong 1998; Yumul et al. 2008; Jian et al. 2008, 2009a, b). Jian et al. (1998) reported a Late Devonian age (362 ± 41 Ma) for a gabbro sample from the ophiolite in the Shuanggou area. Samples of diabase and plagiogranite from the same area yield more precise SHRIMP zircon U–Pb ages of 382.9 ± 3.9 and 375.9 ± 4.2 Ma, respectively (Jian et al. 2009b). Their similar emplacement ages and geochemical signatures indicate that sea-floor spreading already existed in the Middle Devonian (Jian et al. 2009a, b). The sedimentary fragments of different ages from Silurian–early Permian and were deposited in a range of environments, including a deep-marine setting in a rifted continental margin, a shallow-marine setting, and on the ocean floor (Jian et al. 2009a; Xia et al. 2015).

The western Ailaoshan volcanic arc is represented by the middle Permian Yaxuanqiao basalts, andesites, and volcaniclastic rocks (Jian et al. 2009b; Fan et al. 2010; Liu et al. 2011). The linear distribution of the arc to the west of the Ailaoshan suture zone suggests westward subduction of the Ailaoshan oceanic crust. The Early Triassic Lvchun rhyolites formed in a transitional setting between a mature arc and continent–continent collision (Liu et al. 2011). The Early Triassic high-K peraluminous granitoids in the Xin'anzhai and Pinghe areas to the west of the Ailaoshan suture zone formed in a syn-collisional setting (Liu et al. 2015a; Lai et al. 2014a). Late Triassic continental red beds and other clastic rocks are widespread in this region, and they are folded with steeply dipping axial planar cleavages and cut by thrust faults that strike NW to NNW (Fig. 3f).

The Ailaoshan suture zone is located west of the high-grade metamorphic belt (Wang et al. 2014) and is slightly oblique to the trend of the belt (Chung et al. 1997; Figs. 1, 2). Numerous small bodies of ultramafic–mafic rocks occur in the high-grade metamorphic belt (Fig. 2). These lithological and structural relationships indicate that part of the Ailaoshan suture zone underwent significant transformation and destruction during left-lateral shearing along the ASRR shear zone.

Of note, many Early–Middle Triassic granitoids are exposed to the east of the Ailaoshan suture zone. Those within the high-grade metamorphic belt were transformed into mylonites and are strongly foliated (Fig. 3g), such as in the areas of southern Diancangshan (Li et al. 2008; Lin et al. 2012), Yuanjiang (Qi et al. 2010; Lin et al. 2012), Yuanyang (Wang et al. 2013c; this study), Majie, and Yinjie (this study). However, the S-type Heping granite (ca. 244 Ma; Lai et al. 2014b), also known as the Tongtiange granite (ca. 247 Ma; Liu et al. 2015a), in the low-grade metamorphic belt has experienced weak shearing, as only a weak foliation is observed along the northeastern margins of the granitic intrusions (Fig. 3h).

Sample descriptions and analytical techniques

Sample descriptions

Four granitoid samples from the Ailaoshan high-grade metamorphic belt were selected for geochronological and geochemical analyses. The granitoids were emplaced into Proterozoic high-grade metamorphic rocks. Tertiary shearing along the ASRR shear zone transformed the granitoids into mylonitic rocks that exhibit ubiquitous foliations, stretching lineations, and numerous kinematic indicators. The microstructures in the granitoids analyzed in this study are characteristic of medium- to high-grade mylonitization as defined by Trouw et al. (2010). The granitoids have experienced intense superimposition of a major low-temperature shearing event over an earlier high-temperature deformation fabric. Sample locations are shown in Fig. 2a.

Sample ALN13149 (24°48′9.6″N, 100°48′16.9″E) is a fine- to medium-grained, dark gray biotite granitic mylonite from northeast of Yinjie Village. This sample consists mainly of K-feldspar (20–25 %), plagioclase (30–35 %), quartz (25–30 %) and biotite (10 %), with accessory zircon, apatite, and opaque minerals. Feldspar porphyroclasts are almost lens-shaped and are surrounded by a matrix of recrystallized grains that formed mainly by subgrain rotation recrystallization, resulting in a core–mantle structure (Fig. 4a). Intragranular fractures in feldspar indicate the superimposition of subsequent low-temperature shearing (Fig. 4b). Quartz grains have been strongly deformed into ribbons that have largely recrystallized into smaller grains through subgrain rotation recrystallization. The long axes of the grains are parallel to the foliation. The biotite grains have been transformed into very small grains in the matrix and define the main foliation in the mylonitic rocks (Fig. 4a, b).

Sample ALN13178 (24°53′39.7″N, 100°51′29.9″E) is a fine- to medium-grained, light gray muscovite granitic mylonite from southwest of Majie Village. The mylonite consists mainly of K-feldspar (30–40 %), plagioclase (10–15 %), quartz (30–40 %), and muscovite (~ 10 %), along with accessory zircon and apatite. Lenticular feldspar grains have experienced extensive recrystallization and exhibit core–mantle structures (Fig. 4c). Subgrain rotation

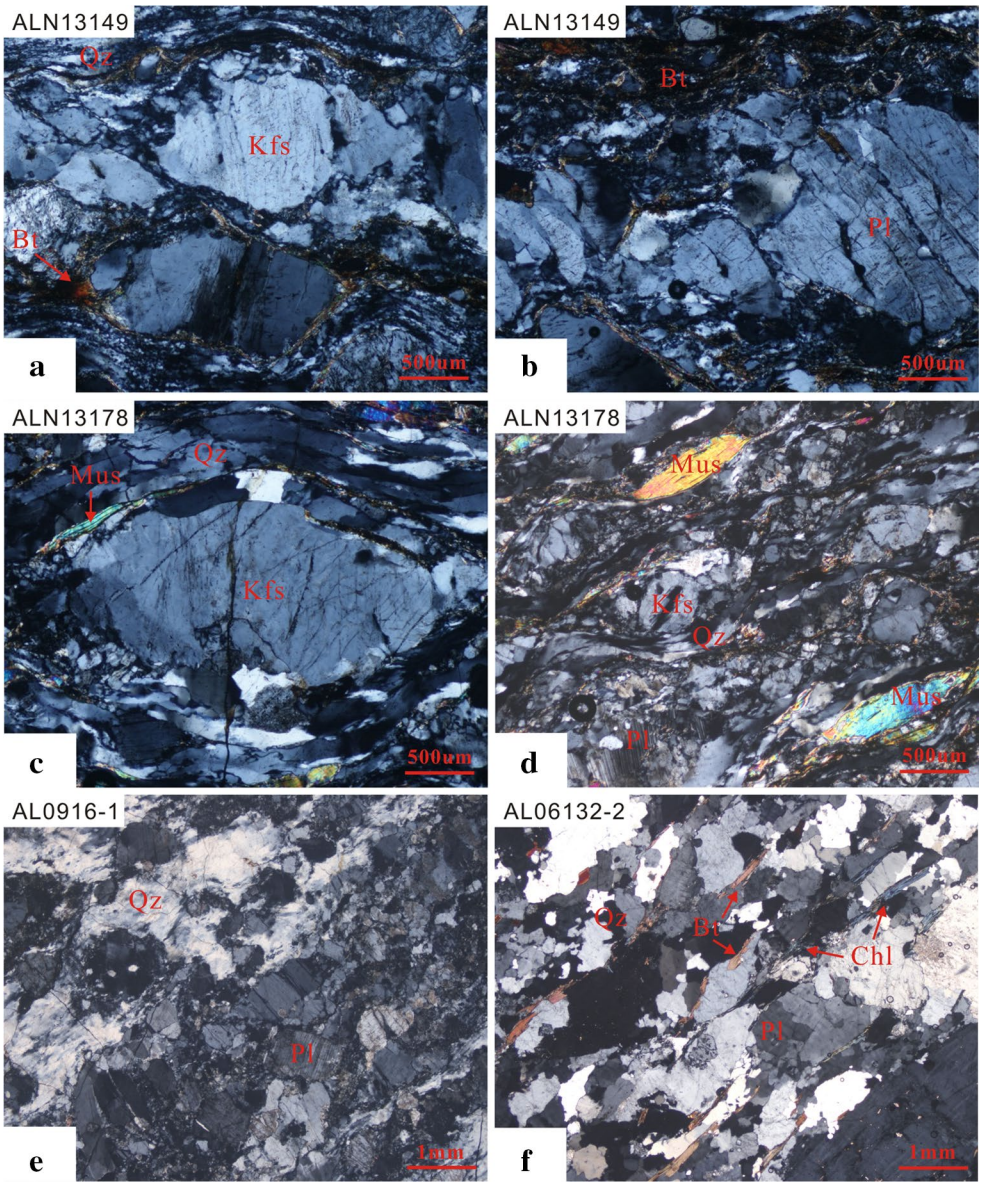

Fig. 4 Microphotos showing mineral compositions and microstructures of granitoids from the Ailaoshan high-grade metamorphic belt. **a** Lenticular feldspar grains surrounded by matrix of recrystallized grains; **b** feldspar with intragranular fractures and fine grained biotite; **c** elongated quartz and feldspar subgrains around the feldspar core, showing core-mantle structure; **d** quartz ribbon, irregular feldspar and muscovite fish in granitic mylonite; **e** lobate quartz and irregular feldspar with intragranular fractures; **f** elongated feldspar and quartz grains orientated parallel to the foliation defined by biotites and chlorites; *Qz* quartz, *Kfs* K-feldspar, *Pl* plagioclase, *Bi* biotite, *Mus* muscovite, *Chl* chlorite

recrystallization was the main deformation mechanism that affected feldspar. Quartz grains occur as ribbons that anastomose around feldspar porphyroclasts and show undulose extinction due to low-temperature crystal plastic deformation (Fig. 4c, d). Serrated quartz grain boundaries indicate high-temperature grain boundary migration recrystallization. Muscovite fish are commonly observed in thin sections (Fig. 4d). The fine muscovite grains and quartz ribbons define the mylonitic foliation (Fig. 4d).

Sample AL0916-1 (24°52′41.2″N, 100°47′33.6″E) was also collected from southwest of Majie Village. This rock is a medium-grained, light gray granitic mylonite that consists mainly of plagioclase (40–50 %), K-feldspar (10–15 %), quartz (25–30 %) and a minor amount of mica. Fine feldspar grains formed by subgrain rotation recrystallization. Intragranular fractures in remnant feldspar crystals and the sub-granular shapes of lobate quartz grains indicate a subsequent low-temperature deformation event (Fig. 4e).

Sample AL06132-2 (23°32′56.3″N, 100°55′05.6″E) is a medium-grained biotite granitic mylonite from southwest of Yuanyang. It mainly consists of K-feldspar (25–30 %), plagioclase (30–35 %), quartz (20–25 %), biotite (5 %), and chlorite (3 %), with accessory zircon, apatite, and opaque minerals. Elongate feldspar and quartz grains are orientated parallel to the foliation, which is also defined by biotite (Fig. 4f). Subgrain rotation recrystallization of feldspar and grain boundary migration of quartz suggest high-temperature deformation. Some biotite grains have been replaced by chlorite during later retrograde metamorphism (Fig. 4f).

Analytical techniques

Zircon grains were separated from the samples using standard density liquid and magnetic separation procedures, followed by handpicking under a binocular microscope. The grains were mounted in epoxy and polished down to expose the grain centers. Cathodoluminescence (CL) images combined with transmitted and reflected light images were used to select the suitable grains and sites for *in suit* analysis.

Zircon LA–ICP–MS U–Pb dating of sample ALN13149 and sample ALN13178 were carried out using a Thermo Finnigan Neptune MC–ICP–MS machine equipped with a Newwave UP 213 laser ablation system at the Institute of Mineral Resources, China Academy of Geological Sciences, Beijing. The laser beam used had a repetition rate of 10 Hz and a spot size of 30 or 40 μm in diameter. Zircon GJ1 was used as external standard for U–Pb dating and was analyzed twice every 10 analyses. The detailed analytical procedures are the same as description by Hou et al. (2009).

Zircons from sample AL0916-1 were analyzed by using LA–ICP–MS at the State Key Laboratory of Geological Processes and Mineral Resources, China University of Geosciences, Wuhan. Laser sampling was performed using a GeoLas 2005 system. An Agilent 7500a ICP-MS instrument was used to acquire ion-signal intensities. Zircon 91500 was used as external standard for U–Pb dating and was analyzed twice every five analyses. GJ-1 and Plesovice were applied as the quality control. Detailed operating conditions for the laser ablation system and the ICP–MS instrument and data reduction are similar to those described by Liu et al. (2008b, 2010).

The LA–ICP–MS analyses of sample AL06132-2 were carried out at the Institute of Geology and Geophysics, Chinese Academy of Sciences, Beijing. An Agilent 7500a quadrupole ICP–MS equipped with 193 nm excimer ArF laser ablation system (GeoLas Plus) was used for U–Pb isotope analyses. Zircon 91500 was used as an external standard for age calculation. The detailed analytical procedure refers to Xie et al. (2008).

Concordia diagrams and weighted mean calculations were made by using Isoplot/Ex_ver3.

In suit zircon Lu–Hf isotopic analysis of sample ALN13149 and sample ALN13178 were carried out by using a Newwave UP 213 laster ablation microprobe, attached to a Neptune MC–ICP–MS at the Institute of Mineral Resources, China Academy of Geological Sciences, Beijing. The beam diameters were 44 or 60 μm depending on the size of ablated domains. Helium was used as carrier gas to transport the ablated sample from the laser ablation cell to the ICP–MS torch via a mixing chamber mixed with Argon. Zircon GJ1 and Plesovice were used as the reference standards during our routine analyses, with a weighted mean $^{176}Hf/^{177}Hf$ ratio of 0.282008 ± 0.000025 (2σ, $n = 26$) (Hou et al. 2007). The instrumental conditions and analytical procedures were comprehensively described by Hou et al. (2007).

In situ zircon Hf isotopic analyses of sample AL06132-2 were conducted using a Neptune MC–ICP–MS, equipped with a 193 nm laser, at the Institute of Geology and Geophysics, Chinese Academy of Sciences in Beijing, China. The spot sizes were either 32 or 63 μm. The detailed analytical technique was described in Wu et al. (2006).

Initial $^{176}Hf/^{177}Hf$ ratios $\varepsilon_{Hf}(t)$ are calculated with reference to the chondritic reservoir (CHUR) of Blichert-Toft and Albarede (1997) at the time of zircon growth from the magma. The single-stage Hf model age (tDM1) is calculated relative to the depleted mantle with present-day $^{176}Hf/^{177}Hf = 0.28325$ and $^{176}Lu/^{177}Hf = 0.0384$ (e.g., Griffin et al. 2000). Two-stage model ages (t_{DM}^{C}) are calculated for the source rock of the magma by assuming a mean $^{176}Lu/^{177}Hf$ value of 0.015 for the average continental crust (Griffin et al. 2002).

Results

Zircon U–Pb ages

The zircon LA–ICP–MS data are listed in Table 1. Representative cathodoluminescence (CL) images and concordant U–Pb data from the analyzed zircons are shown in Fig. 5.

Zircon grains from sample ALN13149 are euhedral, translucent, and prismatic. The grains are generally 80–150 μm in length and have aspect ratios of 1.5–2.5 (Fig. 5a). All the grains show well-developed oscillatory zoning in CL images, suggesting a magmatic origin. Seventeen dated grains have Th and U contents of 65–235 and 123–390 ppm, respectively, and Th/U ratios of 0.51–0.68, also supporting a magmatic origin. The analyses yield a concordant cluster of analyses with a weighted mean

Table 1 Zircon LA–ICP–MS U–Pb date of the granitoids from the Ailaoshan high-grade metamorphic belt

Spot	Pb ($\times10^{-6}$)	Th ($\times10^{-6}$)	U ($\times10^{-6}$)	Th/U	Isotopic ratio						Age (Ma)			
					$^{207}Pb/^{206}Pb$	±1σ	$^{207}Pb/^{235}U$	±1σ	$^{206}Pb/^{238}U$	±1σ	$^{207}Pb/^{235}U$	±1σ	$^{206}Pb/^{238}U$	±1σ
ALN13149, 17 effective data														
02	10.53	127.08	231.04	0.55	0.0531	0.0061	0.2778	0.0323	0.0378	0.0009	248.9	25.64	239.0	5.80
04	17.58	206.22	384.07	0.54	0.0540	0.0024	0.2817	0.0120	0.0383	0.0006	252.0	9.51	242.3	3.51
05	10.16	110.71	217.24	0.51	0.0526	0.0026	0.2842	0.0148	0.0391	0.0007	254.0	11.70	247.1	4.34
06	15.62	192.33	299.74	0.64	0.0501	0.0025	0.2696	0.0132	0.0396	0.0007	242.3	10.58	250.1	4.40
07	7.92	105.88	179.29	0.59	0.0588	0.0039	0.3118	0.0204	0.0384	0.0007	275.6	15.82	243.0	4.08
08	11.52	140.45	256.89	0.55	0.0551	0.0025	0.3009	0.0133	0.0399	0.0006	267.1	10.40	252.3	3.46
10	12.19	175.12	276.08	0.63	0.0533	0.0028	0.2862	0.0138	0.0396	0.0006	255.5	10.91	250.2	3.68
11	11.67	169.07	264.71	0.64	0.0549	0.0030	0.2945	0.0159	0.0389	0.0006	262.1	12.48	245.9	3.65
12	5.56	74.61	127.15	0.59	0.0572	0.0035	0.3069	0.0176	0.0395	0.0006	271.8	13.67	249.7	3.94
13	10.45	137.73	241.62	0.57	0.0531	0.0042	0.2780	0.0186	0.0388	0.0007	249.1	14.77	245.5	4.59
14	14.48	221.54	328.19	0.68	0.0508	0.0023	0.2696	0.0116	0.0388	0.0006	242.4	9.27	245.6	3.63
15	5.29	64.85	123.23	0.53	0.0564	0.0032	0.3099	0.0195	0.0397	0.0008	274.1	15.13	250.9	5.16
16	12.66	166.93	293.89	0.57	0.0534	0.0033	0.2820	0.0171	0.0389	0.0007	252.3	13.58	246.2	4.52
17	9.18	112.25	214.70	0.52	0.0582	0.0056	0.2930	0.0231	0.0389	0.0009	260.9	18.12	246.1	5.71
18	10.76	150.27	254.37	0.59	0.0515	0.0031	0.2705	0.0159	0.0387	0.0009	243.1	12.68	244.6	5.53
19	16.39	202.76	389.71	0.52	0.0530	0.0025	0.2797	0.0122	0.0395	0.0007	250.4	9.65	249.8	4.12
20	15.96	235.17	370.57	0.63	0.0548	0.0030	0.2891	0.0159	0.0392	0.0008	257.8	12.54	248.1	4.76
ALN13178, 41 effective data														
01	16.65	106.42	412.49	0.26	0.0477	0.0035	0.2476	0.0190	0.0378	0.0007	224.7	15.47	239.4	4.41
02	31.05	196.09	365.36	0.54	0.0559	0.0018	0.5698	0.0182	0.0744	0.0009	457.9	11.80	462.3	5.45
03	16.22	86.36	408.28	0.21	0.0510	0.0039	0.2623	0.0192	0.0379	0.0009	236.5	15.42	239.6	5.49
04	27.04	134.78	699.23	0.19	0.0475	0.0032	0.2459	0.0174	0.0376	0.0007	223.2	14.15	237.9	4.26
05	92.23	2241.52	1775.76	1.26	0.0512	0.0016	0.2689	0.0075	0.0384	0.0005	241.8	5.98	242.9	3.30
06	142.21	268.65	410.70	0.65	0.0990	0.0017	3.8855	0.0773	0.2833	0.0030	1610.7	16.08	1607.9	14.97
07	28.52	263.31	316.32	0.83	0.0585	0.0026	0.6008	0.0279	0.0745	0.0011	477.7	17.70	462.9	6.63
08	34.19	58.10	458.69	0.13	0.0590	0.0022	0.6080	0.0242	0.0745	0.0013	482.3	15.27	463.5	7.82
09	153.71	396.10	501.16	0.79	0.0907	0.0018	3.1599	0.0636	0.2534	0.0036	1447.4	15.51	1455.8	18.29
10	43.32	33.00	352.46	0.09	0.0642	0.0025	1.0739	0.0403	0.1210	0.0019	740.7	19.73	736.2	11.13
11	33.86	146.63	861.58	0.17	0.0524	0.0036	0.2704	0.0190	0.0375	0.0010	243.0	15.16	237.1	6.08
12	41.43	79.01	317.64	0.25	0.0634	0.0025	1.0670	0.0396	0.1217	0.0014	737.3	19.46	740.6	7.81
13	11.41	39.06	140.02	0.28	0.0642	0.0080	0.6522	0.0787	0.0743	0.0021	509.8	48.39	461.8	12.73
14	51.24	156.00	1347.02	0.12	0.0515	0.0015	0.2701	0.0093	0.0378	0.0006	242.8	7.41	239.2	3.85
15	14.52	62.72	356.32	0.18	0.0563	0.0052	0.2936	0.0273	0.0378	0.0007	261.4	21.47	239.3	4.46

Table 1 continued

Spot	Pb ($\times10^{-6}$)	Th ($\times10^{-6}$)	U ($\times10^{-6}$)	Th/U	Isotopic ratio						Age (Ma)			
					$^{207}Pb/^{206}Pb$	±1σ	$^{207}Pb/^{235}U$	±1σ	$^{206}Pb/^{238}U$	±1σ	$^{207}Pb/^{235}U$	±1σ	$^{206}Pb/^{238}U$	±1σ
16	192.94	421.19	1409.44	0.30	0.0684	0.0035	1.1496	0.0625	0.1212	0.0033	777.0	29.52	737.5	19.23
17	121.94	478.26	665.20	0.72	0.0718	0.0020	1.4473	0.0413	0.1454	0.0019	908.8	17.15	875.1	10.78
18	25.51	105.39	621.00	0.17	0.0571	0.0025	0.2979	0.0128	0.0383	0.0009	264.8	10.02	242.6	5.46
19	14.91	63.58	356.52	0.18	0.0490	0.0031	0.2539	0.0157	0.0378	0.0007	229.7	12.69	239.1	4.48
20	15.45	126.99	219.30	0.58	0.0544	0.0031	0.4177	0.0224	0.0561	0.0012	354.4	16.03	352.1	7.25
21	249.78	70.45	500.16	0.14	0.1651	0.0029	9.2582	0.1805	0.4045	0.0050	2363.9	17.87	2189.8	22.95
22	23.23	81.51	558.71	0.15	0.0516	0.0026	0.2639	0.0132	0.0374	0.0007	237.8	10.64	236.4	4.29
23	36.13	128.12	877.04	0.15	0.0500	0.0025	0.2551	0.0113	0.0375	0.0008	230.7	9.17	237.1	5.18
24	4.35	15.80	28.96	0.55	0.0701	0.0067	1.1659	0.1222	0.1218	0.0035	784.7	57.35	740.9	20.04
25	86.29	489.44	945.91	0.52	0.0544	0.0014	0.5613	0.0154	0.0747	0.0010	452.4	10.03	464.3	6.15
26	32.23	164.27	760.78	0.22	0.0485	0.0016	0.2544	0.0088	0.0380	0.0005	230.1	7.13	240.2	3.16
27	51.28	94.55	1222.91	0.08	0.0523	0.0016	0.2771	0.0091	0.0384	0.0006	248.4	7.20	242.8	4.00
28	55.09	128.91	87.63	1.47	0.1603	0.0062	8.9029	0.2935	0.4046	0.0091	2328.1	30.10	2190.1	41.57
29	15.65	103.00	369.71	0.28	0.0529	0.0032	0.2717	0.0159	0.0375	0.0005	244.0	12.66	237.6	3.20
30	8.54	23.99	56.99	0.42	0.0782	0.0080	1.2630	0.1108	0.1236	0.0037	829.3	49.77	751.2	21.12
31	29.59	130.87	783.72	0.17	0.0538	0.0033	0.2861	0.0186	0.0384	0.0007	255.5	14.72	242.7	4.65
32	18.71	83.55	277.58	0.30	0.0608	0.0048	0.5278	0.0396	0.0639	0.0019	430.3	26.33	399.5	11.78
33	27.13	91.77	274.56	0.33	0.0637	0.0031	0.8344	0.0521	0.0955	0.0041	616.1	28.87	588.2	23.98
36	37.59	130.57	1056.19	0.12	0.0531	0.0034	0.2760	0.0180	0.0378	0.0006	247.5	14.36	239.4	3.56
37	46.73	76.02	798.23	0.10	0.0518	0.0035	0.4532	0.0313	0.0635	0.0015	379.5	21.88	397.2	9.20
39	33.83	127.27	955.85	0.13	0.0524	0.0020	0.2698	0.0103	0.0376	0.0006	242.5	8.23	238.2	3.87
41	22.27	57.08	143.71	0.40	0.0703	0.0036	1.4750	0.0736	0.1525	0.0023	920.2	30.20	914.8	13.14
42	54.24	87.87	930.28	0.09	0.0561	0.0025	0.4888	0.0216	0.0632	0.0011	404.1	14.71	394.8	6.53
43	89.91	82.25	784.07	0.10	0.0676	0.0017	1.1442	0.0351	0.1221	0.0021	774.5	16.63	742.5	11.90
44	116.09	270.02	364.02	0.74	0.0922	0.0029	3.6054	0.1101	0.2829	0.0045	1550.7	24.27	1606.2	22.41
45	28.19	100.13	773.25	0.13	0.0555	0.0020	0.2873	0.0105	0.0378	0.0005	256.5	8.24	239.0	3.37
AL0916-1, 19 effective data														
01	151.53	1427.33	3250.43	0.44	0.0514	0.0005	0.2723	0.0026	0.0383	0.0001	245	2	242	1
02	24.85	227.09	538.55	0.42	0.0523	0.0013	0.2772	0.0066	0.0383	0.0003	248	5	243	2
03	53.42	285.40	1229.24	0.23	0.0509	0.0010	0.2716	0.0063	0.0386	0.0005	244	5	244	3
04	71.90	723.50	1543.21	0.47	0.0512	0.0008	0.2732	0.0047	0.0385	0.0003	245	4	244	2
05	94.97	989.26	2037.92	0.49	0.0491	0.0008	0.2576	0.0042	0.0379	0.0002	233	3	240	1
07	62.15	426.06	1395.17	0.31	0.0490	0.0008	0.2607	0.0042	0.0385	0.0003	235	3	244	2
08	52.67	523.98	1137.62	0.46	0.0504	0.0008	0.2687	0.0048	0.0385	0.0004	242	4	244	3
09	13.29	108.38	289.61	0.37	0.0526	0.0016	0.2782	0.0080	0.0385	0.0003	249	6	243	2

Table 1 continued

Spot	Pb ($\times10^{-6}$)	Th ($\times10^{-6}$)	U ($\times10^{-6}$)	Th/U	Isotopic ratio						Age (Ma)			
					$^{207}Pb/^{206}Pb$	±1σ	$^{207}Pb/^{235}U$	±1σ	$^{206}Pb/^{238}U$	±1σ	$^{207}Pb/^{235}U$	±1σ	$^{206}Pb/^{238}U$	±1σ
10	34.82	341.65	759.86	0.45	0.0509	0.0011	0.2644	0.0062	0.0376	0.0003	238	5	238	2
11	169.05	1195.78	3815.46	0.31	0.0500	0.0008	0.2659	0.0056	0.0385	0.0006	239	5	244	4
12	85.54	632.15	1918.04	0.33	0.0509	0.0008	0.2687	0.0043	0.0382	0.0002	242	3	241	1
13	90.99	758.66	2048.27	0.37	0.0528	0.0020	0.2770	0.0132	0.0375	0.0004	248	10	238	2
14	208.99	1810.43	4549.46	0.40	0.0507	0.0007	0.2706	0.0037	0.0386	0.0002	243	3	244	1
15	128.45	1282.77	2718.38	0.47	0.0503	0.0008	0.2679	0.0044	0.0385	0.0003	241	3	243	2
16	97.56	687.13	2184.47	0.31	0.0508	0.0008	0.2708	0.0045	0.0385	0.0003	243	4	244	2
17	43.08	386.22	940.42	0.41	0.0519	0.0011	0.2689	0.0056	0.0375	0.0003	242	4	237	2
18	109.24	890.19	2448.68	0.36	0.0512	0.0007	0.2681	0.0037	0.0378	0.0002	241	3	239	1
19	201.37	1878.56	4428.89	0.42	0.0502	0.0007	0.2633	0.0035	0.0378	0.0002	237	3	239	1
20	175.40	1159.74	3975.36	0.29	0.0525	0.0016	0.2781	0.0080	0.0385	0.0004	249	6	243	2
AL06132-2, 29 effective data														
01	40.43	57.16	211.81	0.27	0.0502	0.0015	0.2937	0.0083	0.0425	0.0007	261	6	268	5
02	32.79	54.12	209.57	0.26	0.0509	0.0023	0.2569	0.0104	0.0366	0.0008	232	8	232	5
03	34.04	53.90	180.32	0.30	0.0504	0.0020	0.2885	0.0105	0.0415	0.0008	257	8	262	5
04	49.02	56.83	291.46	0.19	0.0488	0.0018	0.2606	0.0087	0.0387	0.0007	235	7	245	5
05	34.89	54.73	193.54	0.28	0.0482	0.0022	0.2576	0.0107	0.0388	0.0009	233	9	245	5
06	54.88	53.06	292.72	0.18	0.0512	0.0021	0.2985	0.0113	0.0422	0.0009	265	9	267	6
07	49.98	60.43	303.54	0.20	0.0511	0.0021	0.2560	0.0096	0.0363	0.0008	231	8	230	5
08	35.06	58.22	205.35	0.28	0.0524	0.0022	0.2790	0.0105	0.0386	0.0008	250	8	244	5
09	17.73	16.40	50.22	0.33	0.0581	0.0028	0.6281	0.0282	0.0784	0.0019	495	18	487	12
10	153.84	70.53	321.69	0.22	0.0582	0.0010	0.8798	0.0140	0.1096	0.0015	641	8	670	9
11	39.18	54.84	234.59	0.23	0.0513	0.0017	0.2695	0.0083	0.0381	0.0007	242	7	241	4
12	34.97	53.36	51.63	1.03	0.0675	0.0022	1.2793	0.0380	0.1373	0.0028	837	17	829	16
13	58.03	56.24	342.27	0.16	0.0509	0.0016	0.2662	0.0077	0.0379	0.0007	240	6	240	4
14	50.68	65.04	285.84	0.23	0.0519	0.0016	0.2979	0.0083	0.0416	0.0007	265	7	263	4
15	55.34	60.82	351.95	0.17	0.0501	0.0019	0.2528	0.0086	0.0366	0.0007	229	7	232	4
16	55.43	61.21	359.47	0.17	0.0504	0.0012	0.2501	0.0055	0.0360	0.0005	227	4	228	3
17	35.36	57.69	196.55	0.29	0.0534	0.0015	0.3029	0.0080	0.0412	0.0007	269	6	260	4
18	40.43	46.40	247.91	0.19	0.0525	0.0014	0.2748	0.0070	0.0379	0.0006	247	6	240	4
19	34.14	78.19	198.22	0.39	0.0549	0.0022	0.2918	0.0104	0.0386	0.0008	260	8	244	5
20	39.25	69.25	242.31	0.29	0.0504	0.0015	0.2586	0.0073	0.0372	0.0006	234	6	236	4
22	50.12	64.50	311.49	0.21	0.0547	0.0017	0.2802	0.0078	0.0371	0.0007	251	6	235	4
23	57.74	71.09	355.51	0.20	0.0521	0.0015	0.2764	0.0072	0.0385	0.0006	248	6	243	4
24	96.31	101.44	388.59	0.26	0.0565	0.0022	0.4737	0.0166	0.0608	0.0013	394	11	380	8

Table 1 continued

Spot	Pb ($\times 10^{-6}$)	Th ($\times 10^{-6}$)	U ($\times 10^{-6}$)	Th/U	Isotopic ratio						Age (Ma)			
					$^{207}Pb/^{206}Pb$	±1σ	$^{207}Pb/^{235}U$	±1σ	$^{206}Pb/^{238}U$	±1σ	$^{207}Pb/^{235}U$	±1σ	$^{206}Pb/^{238}U$	±1σ
25	389.22	96.54	572.92	0.17	0.0698	0.0008	1.5177	0.0158	0.1576	0.0020	938	6	944	11
26	39.61	55.67	232.99	0.24	0.0517	0.0023	0.2712	0.0113	0.0380	0.0008	244	9	241	5
27	35.30	72.86	208.89	0.35	0.0533	0.0017	0.2764	0.0081	0.0376	0.0007	248	6	238	4
28	46.06	59.97	281.48	0.21	0.0514	0.0015	0.2726	0.0072	0.0385	0.0006	245	6	244	4
29	69.30	77.24	419.53	0.18	0.0514	0.0022	0.2667	0.0107	0.0376	0.0008	240	9	238	5
30	61.03	71.15	383.13	0.19	0.0514	0.0015	0.2665	0.0072	0.0376	0.0006	240	6	238	4

$^{206}Pb/^{238}U$ age of 247.1 ± 2.0 Ma (2σ, MSWD = 0.65) (Fig. 5b).

Zircon grains from sample ALN13178 are translucent and occur as prismatic crystals with rounded, short or somewhat irregular shapes. The grains are generally 60–120 μm long and have aspect ratios of 1.5–2 (Fig. 5c). Three types of zircon grains are identified based on structural zoning. Most grains have a core–rim structure in which the rims exhibit well-developed oscillatory zoning, whereas the cores either have oscillatory zoning or are homogenously dark gray. The remaining grains generally exhibit well-developed oscillatory zoning. The occurrence of oscillatory zoning in zircon rims and whole zircon grains indicates that they are of magmatic origin. The zircon cores are interpreted to be inherited zircon grains. Forty-five analyses were performed on 30 zircon grains, of which 43 analyses were considered reliable. The dated grains have Th and U contents of 16–489 and 29–1776 ppm, respectively, with an exception of spot 5, which has a Th content of 2242 ppm. The Th/U ratios are between 0.12 and 1.47. Forty-one analyses are concordant in the U–Pb concordia diagram and yield ages of 1607.9–236.4 Ma, including four age groups with weighted mean ages of 239.5 ± 1.8 Ma (2σ, MSWD = 0.22), 396.3 ± 9.5 Ma (2σ, MSWD = 0.069), 463.1 ± 6.0 Ma (2σ, MSWD = 0.018), and 740.4 ± 9.9 Ma (2σ, MSWD = 0.092) (Fig. 5d). Spots 21 and 28 are discordant and yield significantly older ages of 2190 ± 23 and 2190 ± 42 Ma, respectively.

Zircon grains from sample AL0916-1 are nearly translucent and occur as euhedral prismatic crystals. They range in size from 80 to 200 μm, with aspect ratios of 0.8–2.0. CL images of zircon grains reveal well-developed oscillatory zoning (Fig. 5e), suggesting a magmatic origin. Nineteen effectively dated grains have Th and U contents of 227–1810 and 290–4549 ppm, respectively, and Th/U ratios are between 0.23 and 0.49. The analyses yield a concordant cluster of ages with a weighted mean $^{206}Pb/^{238}U$ age of 241.2 ± 1.0 Ma (2σ, MSWD = 2.3) (Fig. 5f).

Most of the zircon grains from sample AL06132-2 are euhedral, translucent, and prismatic. The grains are commonly 120–300 μm long and have aspect ratios of up to 3.0 (Fig. 5g). They exhibit oscillatory zoning and some grains exhibit core–rim structures that have a dark core in CL images. Twenty-nine effectively dated grains have Th and U contents of 16–101 ppm and 50–573 ppm, respectively. The Th/U ratios are between 0.16 and 0.39, except for spot 12, which has a Th/U ratio of 1.03. All analyzed spots are concordant or nearly concordant, yielding ages between 944 and 228 Ma. Analyses of the rims yield two concordant age populations of 263.4 ± 4.1 and 237.9 ± 2.6 Ma (2σ, MSWD = 1.7) (Fig. 5h). The cores yield several older ages (e.g., 994 ± 11, 829 ± 16, 670 ± 9, 487 ± 12, and 380 ± 8 Ma).

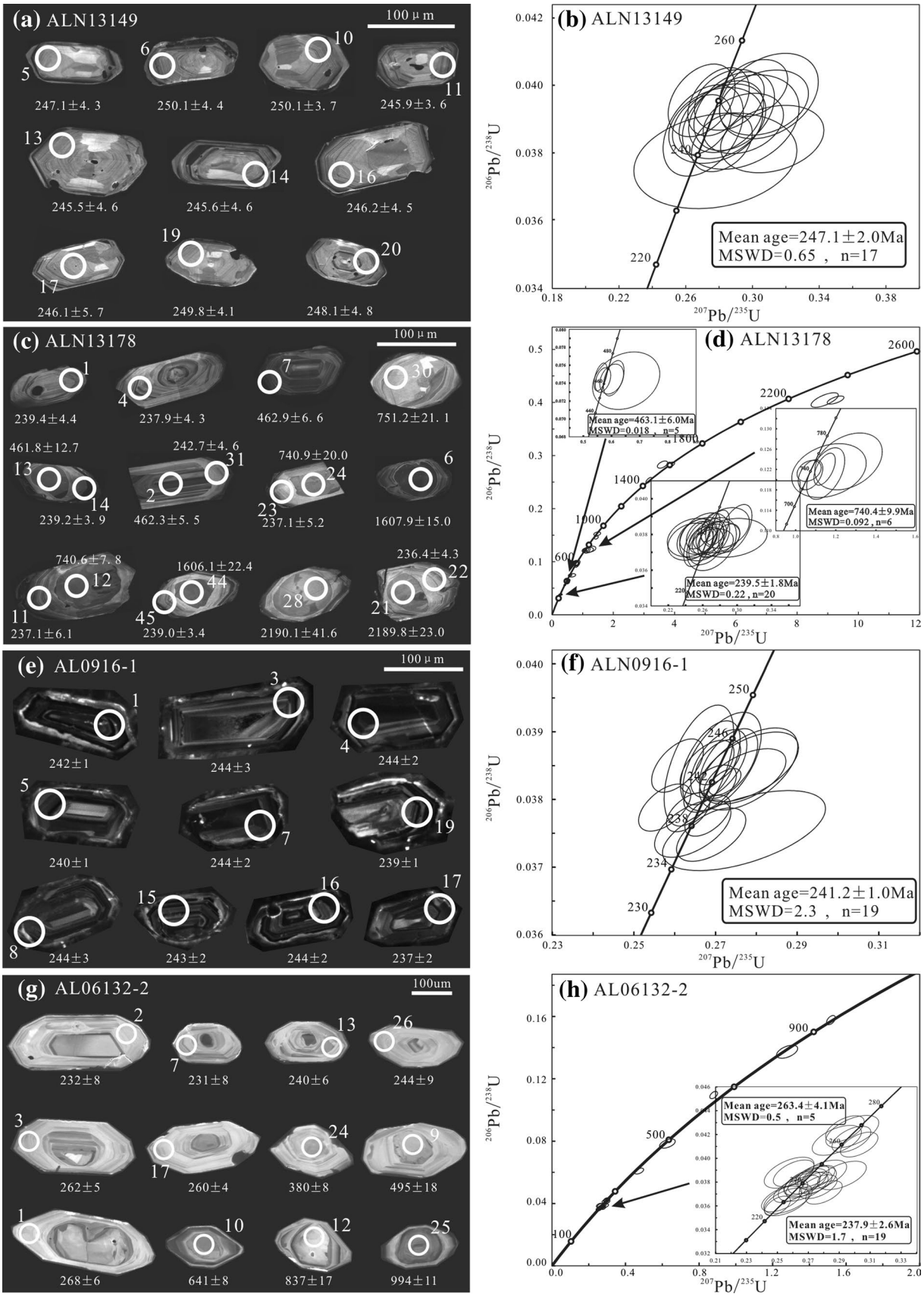

Fig. 5 CL images of representative zircon grains (**a**, **c**, **e**, **g**) and U–Pb Concordia diagram for zircon grains (**b**, **d**, **f**, **h**)

Zircon Hf isotopes

A total of 80 dated zircon grains from three samples were analyzed for $^{176}Hf/^{177}Hf$ isotopic ratios. The results are listed in Table 2. Initial $^{176}Hf/^{177}Hf$ ratios and $\varepsilon_{Hf}(t)$ values were calculated for their respective U–Pb ages.

Ten dated zircon grains from sample ALN13178 yield uniform, strongly positive $\varepsilon_{Hf}(t)$ values ranging from +7.8 to +11.4, and t^{C}_{DM} ages of 775–503 Ma. Forty-one dated zircon grains from sample ALN13178 have Triassic zircon rims that yield negative $\varepsilon_{Hf}(t)$ values of between −20.4 and −5.3, resulting in t^{C}_{DM} ages of 2557–1606 Ma. The inherited zircon cores yield more heterogeneous Hf isotope ratios, with $\varepsilon_{Hf}(t)$ values from −24 to +9.7 and t^{C}_{DM} ages of 3280–1213 Ma. Twenty-nine dated zircon grains from sample AL06132-2 have rims that yield uniformly negative $\varepsilon_{Hf}(t)$ values of −15.3 to −9.0 and t^{C}_{DM} ages of 2228–1842 Ma. Five analyses of inherited zircon cores yield a wide range of $\varepsilon_{Hf}(t)$ values from −17.6 to +3.1, and t^{C}_{DM} ages from 2487 to 1316 Ma.

Discussion

Ailaoshan micro-block

Along the western margin of the Yangtze block, discontinuously exposed late Paleoproterozoic to early Neoproterozoic metamorphosed volcano-sedimentary units and Neoproterozoic plutonic rocks comprise the Precambrian basement of the Yangtze block (Zhou et al. 2002; Sun et al. 2008; Greentree and Li 2008; Zhao et al. 2008, 2010; Zhao and Cawood 2012). The sedimentary cover sequence of the Yangtze Block consists mainly of folded Neoproterozoic to Mesozoic shallow-marine strata (Yan et al. 2003). Triassic strata include both terrestrial and marine sedimentary rocks, whereas Jurassic to Cretaceous strata are mainly terrestrial sediments (BGMRYP 1990).

The Ailaoshan high-grade metamorphic belt contains the oldest rocks in this area and has experienced intense shearing during the Tertiary. Recent studies have revealed that the protoliths of the high-grade metamorphic rocks were complex. Neoproterozoic and early Paleozoic protoliths of sedimentary and igneous origins are widespread (Liu et al. 2008a, b; Qi et al. 2012; Wang et al. 2013c; Cai et al. 2014) and were intruded by many Permo–Triassic granitoids (Li et al. 2008; Qi et al. 2010; Searle et al. 2010; Lin et al. 2012; Lai et al. 2014b; Liu et al. 2014, 2015a). The present study also shows that zircon grains from the Yinjie, Majie, and Yuanjiang granitoids yield Proterozoic and Paleozoic ages (Fig. 6), which is consistent with previous studies. The Triassic ages of four samples are interpreted as the emplacement ages of their magmatic protoliths. The variable inherited zircon U–Pb ages from the Majie and Yuanjiang granitoids indicate a variety of source compositions that likely correspond to the complex source rocks along the high-grade metamorphic belt. The age spectra of inherited and detrital zircon grains from granitoids and meta-sedimentary rocks within the Ailaoshan micro-block are comparable to those from the basement of the Yangtze block (Li et al. 2003; Sun et al. 2009; Liu et al. 2014). Furthermore, the zircon Hf model ages also likely indicate similar source-region compositions to those of the Yangtze block (Fig. 7; Lin et al. 2012; Liu et al. 2014, 2015a; this study).

The low-grade metamorphic belt is dominated by Paleozoic clastic rocks and carbonates that were deformed and metamorphosed during the Indosinian orogeny. The Proterozoic inherited zircon grains and Hf model ages from the Tongtiange pluton are similar to those of the Ailaoshan Proterozoic gneisses, indicating that the Tongtiange granite was sourced from the gneisses (Liu et al. 2015a, b).

The low-grade and high-grade metamorphic belts are characterized by distinct lithological and structural features, which are attributed to their contrasting tectonic histories. The dominant, although slightly oblique, left-lateral shearing along the ASRR shear zone resulted in a southwest-directed thrust fault that juxtaposed the high-grade metamorphic rocks over the low-grade metamorphic rocks. The extensive strike-slip displacement may have produced several kilometers of uplift (Tapponnier et al. 1990). A later stage of right-lateral normal faulting along the Red River Fault to the east of the high-grade metamorphic belt has probably also contributed to the uplift of the massif (Tapponnier et al. 1990; Cao et al. 2011b). The exhumed high-grade metamorphic rocks are probably equivalents of the basement that underlies the low-grade metamorphic belt and the western Yangtze block. Therefore, the evidence discussed above supports the derivation of the Ailaoshan micro-block from the western margin of the Yangtze plate.

Regionally, several micro-blocks are exposed along the western Yangtze margin, such as the Zhongzan block located between the Jinshajiang and Ganzi–Litang suture zones. The Zhongzan block, also called the western Yidun Arc, consists of a Neoproterozoic basement of granitic gneisses and meta-volcanic rocks that are covered by greenschist-facies metamorphic rocks. This cover sequence originated as Paleozoic shallow- to deep-marine carbonates and clastic rocks intercalated with sporadic mafic volcanic rocks (Chang 1997; Wang et al. 2000, 2013a, b). The Neoproterozoic amphibolite-facies Eaqing Complex, which is similar to the Ailaoshan complex, may represent the metamorphic basement of the Jinshajiang area (Wang et al. 2000). Based on stratigraphic comparisons, fossils, and age distribution patterns of detrital zircon grains from the sedimentary rocks, the Zhongzan block

Table 2 Zircon Hf isotopic compositions of granitoids from the Ailaoshan high-grade metamorphic belt

Spot	Age (Ma)	$^{176}Yb/^{177}Hf$	$^{176}Lu/^{177}Hf$	$^{176}Hf/^{177}Hf$	2σ	$(176Hf/177Hf)_i$	$\varepsilon_{Hf}(0)$	$\varepsilon_{Hf}(t)$	t_{DM}	t_{DM}^{C}	$f_{Lu/Hf}$
ALN13149											
05	247.1	0.070317	0.002276	0.282851	0.000025	0.282840	2.8	7.8	589	775	−0.93
06	250.1	0.054016	0.001593	0.282967	0.000018	0.282959	6.9	12.1	411	503	−0.95
10	250.2	0.042921	0.001186	0.282924	0.000020	0.282918	5.4	10.7	467	596	−0.96
11	245.9	0.059843	0.001708	0.282863	0.000018	0.282855	3.2	8.4	561	741	−0.95
13	245.5	0.055689	0.001597	0.282923	0.000020	0.282915	5.3	10.5	474	606	−0.95
14	245.6	0.069552	0.002076	0.282927	0.000018	0.282917	5.5	10.5	475	601	−0.94
16	246.2	0.051395	0.001403	0.282926	0.000018	0.282920	5.4	10.6	467	595	−0.96
17	246.1	0.056006	0.001603	0.282931	0.000016	0.282924	5.6	10.8	462	586	−0.95
19	249.8	0.053781	0.001465	0.282947	0.000020	0.282940	6.2	11.4	437	546	−0.96
20	248.1	0.090738	0.002856	0.282946	0.000024	0.282932	6.1	11.1	457	565	−0.91
ALN13178											
01	239.4	0.100562	0.002789	0.282377	0.000031	0.282364	−14.0	−9.2	1298	1850	−0.92
02	462.3	0.054068	0.001503	0.282291	0.000021	0.282278	−17.0	−7.3	1374	1900	−0.95
03	239.6	0.068457	0.001776	0.282341	0.000026	0.282333	−15.2	−10.3	1313	1920	−0.95
04	237.9	0.058438	0.001523	0.282236	0.000020	0.282229	−18.9	−14.0	1453	2152	−0.95
05	242.9	0.115159	0.003005	0.282314	0.000025	0.282300	−16.2	−11.4	1398	1991	−0.91
06	1607.9	0.096811	0.002775	0.282117	0.000039	0.282033	−23.1	9.7	1676	1712	−0.92
07	462.9	0.050061	0.001379	0.282288	0.000024	0.282276	−17.1	−7.4	1374	1904	−0.96
08	463.5	0.069387	0.002127	0.281825	0.000039	0.281807	−33.5	−24.0	2063	2944	−0.94
09	1455.8	0.029321	0.000805	0.281731	0.000023	0.281709	−36.8	−5.3	2121	2525	−0.98
10	736.2	0.016467	0.000502	0.281850	0.000021	0.281843	−32.6	−16.6	1943	2691	−0.98
11	237.1	0.107341	0.002804	0.282299	0.000024	0.282287	−16.7	−12.0	1412	2024	−0.92
12	740.6	0.037008	0.000911	0.282518	0.000026	0.282506	−9.0	6.9	1035	1213	−0.97
13	461.8	0.009212	0.000250	0.282507	0.000027	0.282505	−9.4	0.7	1033	1394	−0.99
14	239.2	0.116264	0.003618	0.282421	0.000030	0.282405	−12.4	−7.7	1262	1759	−0.89
15	239.3	0.079744	0.002108	0.282314	0.000022	0.282304	−16.2	−11.3	1364	1984	−0.94
16	737.5	0.067195	0.001781	0.282212	0.000019	0.282187	−19.8	−4.4	1497	1927	−0.95
17	875.1	0.031892	0.000867	0.282361	0.000026	0.282346	−14.5	4.3	1254	1483	−0.97
18	242.6	0.068654	0.001774	0.282377	0.000024	0.282369	−14.0	−8.9	1262	1838	−0.95
19	239.1	0.058494	0.001463	0.282235	0.000024	0.282228	−19.0	−14.0	1452	2154	−0.96
20	352.1	0.057626	0.001524	0.282206	0.000028	0.282195	−20.0	−12.7	1496	2155	−0.95
21	2189.8	0.021319	0.000575	0.281172	0.000025	0.281148	−56.6	−8.5	2864	3280	−0.98
22	236.4	0.074868	0.001866	0.282376	0.000022	0.282368	−14.0	−9.1	1266	1844	−0.94
23	237.1	0.122811	0.003499	0.282489	0.000037	0.282474	−10.0	−5.3	1155	1606	−0.89
24	740.9	0.041110	0.001181	0.282447	0.000028	0.282431	−11.5	4.3	1143	1380	−0.96
25	464.3	0.022620	0.000582	0.282172	0.000026	0.282167	−21.2	−11.2	1505	2147	−0.98
26	240.2	0.113261	0.002794	0.282360	0.000023	0.282347	−14.6	−9.7	1323	1887	−0.92
27	242.8	0.031915	0.000749	0.282265	0.000024	0.282262	−17.9	−12.7	1383	2077	−0.98
28	2190.1	0.022253	0.000568	0.281462	0.000032	0.281438	−46.3	1.8	2474	2649	−0.98
29	237.6	0.090596	0.002239	0.282478	0.000026	0.282468	−10.4	−5.5	1131	1619	−0.93
30	751.2	0.034375	0.000924	0.282506	0.000027	0.282493	−9.4	6.7	1053	1234	−0.97
31	242.7	0.125422	0.003724	0.282295	0.000043	0.282278	−16.9	−12.1	1455	2039	−0.89
32	399.5	0.073998	0.002063	0.282435	0.000022	0.282420	−11.9	−3.7	1188	1624	−0.94
33	588.2	0.046218	0.001241	0.282223	0.000026	0.282210	−19.4	−6.9	1460	1972	−0.96
36	239.4	0.048942	0.001292	0.282053	0.000023	0.282047	−25.4	−20.4	1701	2557	−0.96
37	397.2	0.067312	0.002036	0.282234	0.000031	0.282219	−19.0	−10.8	1476	2073	−0.94
39	238.2	0.097873	0.002420	0.282348	0.000023	0.282337	−15.0	−10.2	1327	1912	−0.93

Table 2 continued

Spot	Age (Ma)	$^{176}Yb/^{177}Hf$	$^{176}Lu/^{177}Hf$	$^{176}Hf/^{177}Hf$	2σ	$(176Hf/177Hf)_i$	$\varepsilon_{Hf}(0)$	$\varepsilon_{Hf}(t)$	t_{DM}	t_{DM}^{C}	$f_{Lu/Hf}$
41	914.8	0.031708	0.000827	0.282348	0.000024	0.282334	−15.0	4.7	1271	1487	−0.98
42	394.8	0.088545	0.002210	0.282436	0.000024	0.282420	−11.9	−3.8	1191	1626	−0.93
43	742.5	0.050700	0.001271	0.282254	0.000019	0.282236	−18.3	−2.6	1418	1814	−0.96
44	1606.2	0.034479	0.000855	0.281853	0.000027	0.281827	−32.5	2.3	1956	2168	−0.97
45	239.0	0.083314	0.002089	0.282482	0.000021	0.282473	−10.2	−5.3	1121	1607	−0.94
AL06132-2											
01	268.0	0.035994	0.001369	0.282218	0.000019	0.282211	−19.6	−14.0	1474	2174	−0.96
02	232.0	0.031859	0.001227	0.282234	0.000018	0.282229	−19.0	−14.1	1445	2155	−0.96
03	262.0	0.025539	0.000955	0.282238	0.000018	0.282234	−18.9	−13.3	1430	2127	−0.97
04	245.0	0.035887	0.001344	0.282215	0.000018	0.282209	−19.7	−14.5	1476	2191	−0.96
05	245.0	0.030262	0.001130	0.282217	0.000017	0.282212	−19.6	−14.4	1466	2186	−0.97
06	267.0	0.032601	0.001236	0.282207	0.000017	0.282201	−20.0	−14.3	1484	2196	−0.96
07	230.0	0.039896	0.001524	0.282203	0.000019	0.282197	−20.1	−15.3	1501	2228	−0.95
08	244.0	0.032179	0.001186	0.282217	0.000017	0.282212	−19.6	−14.5	1468	2186	−0.96
09	487.0	0.006884	0.000267	0.282537	0.000017	0.282535	−8.3	2.3	993	1316	−0.99
10	670.0	0.013123	0.000433	0.282025	0.000019	0.282020	−26.4	−11.8	1702	2355	−0.99
11	241.0	0.031262	0.001156	0.282249	0.000017	0.282244	−18.5	−13.4	1422	2117	−0.97
12	829.0	0.028622	0.001153	0.282361	0.000021	0.282343	−14.5	3.1	1265	1532	−0.97
13	240.0	0.037100	0.001328	0.282276	0.000018	0.282270	−17.6	−12.5	1391	2060	−0.96
14	263.0	0.037220	0.001377	0.282198	0.000015	0.282191	−20.3	−14.8	1502	2220	−0.96
15	232.0	0.040865	0.001536	0.282269	0.000018	0.282263	−17.8	−12.9	1408	2081	−0.95
16	228.0	0.039539	0.001455	0.282274	0.000017	0.282268	−17.6	−12.8	1398	2071	−0.96
17	260.0	0.031387	0.001153	0.282238	0.000018	0.282232	−18.9	−13.4	1437	2131	−0.97
18	240.0	0.032204	0.001169	0.282216	0.000015	0.282211	−19.6	−14.6	1468	2190	−0.96
19	244.0	0.035847	0.001328	0.282218	0.000018	0.282212	−19.6	−14.5	1472	2186	−0.96
20	236.0	0.037420	0.001347	0.282200	0.000015	0.282194	−20.2	−15.3	1498	2229	−0.96
22	235.0	0.048467	0.001778	0.282248	0.000016	0.282240	−18.5	−13.7	1447	2129	−0.95
23	243.0	0.057350	0.002127	0.282377	0.000017	0.282367	−14.0	−9.0	1275	1842	−0.94
24	380.0	0.019583	0.000728	0.282044	0.000021	0.282039	−25.7	−17.6	1689	2487	−0.98
25	944.0	0.015187	0.000531	0.282039	0.000017	0.282030	−25.9	−5.4	1687	2163	−0.98
26	241.0	0.033542	0.001214	0.282225	0.000016	0.282220	−19.3	−14.2	1458	2170	−0.96
27	238.0	0.032967	0.001179	0.282240	0.000019	0.282234	−18.8	−13.8	1436	2140	−0.96
28	244.0	0.035358	0.001255	0.282215	0.000018	0.282209	−19.7	−14.6	1474	2192	−0.96
29	238.0	0.063138	0.002246	0.282311	0.000019	0.282301	−16.3	−11.4	1374	1992	−0.93
30	238.0	0.057558	0.002065	0.282304	0.000019	0.282295	−16.5	−11.7	1378	2006	−0.94

is considered to have separated from the western margin of the Yangtze block in response to the formation of the Ganzi–Litang Ocean during the late Permian (Chang 1997; Zhong 1998; Wang et al. 2013a, b). Conversely, the eastern Yidun Arc is composed almost exclusively of Middle–Late Triassic clastic strata and arc-related volcanic and plutonic rocks. However, two peaks in zircon Hf model ages led Peng et al. (2014) to suggest two major episodes of Mesoproterozoic juvenile continental crust development beneath the eastern Yidun arc, which is similarly interpreted for the Yangtze block. Therefore, the basements of the Zhongzan block and the eastern Yidun arc share the same evolutionary history as the Yangtze block during the Mesoproterozoic (Reid et al. 2007; Leng et al. 2014; Peng et al. 2014).

In fact, the Zhongzan block and the eastern Yidun arc are comparable with the Ailaoshan block, except that the Ailaoshan block has experienced intense deformation that resulted from the ASRR shear zone. Another similar example is the Nam Co block (also called the Song Ma structure or the Song Ma anticlinorium) between the Song Da rift and the Song Ma suture zone. This anticlinorial metamorphic complex extends NW–SE across northern Vietnam and is dominated by Neoproterozoic and early to late Paleozoic greenschist- to amphibolite-facies metamorphic rocks (e.g., gneiss, schist, amphibolite, quartzite, and marble; Findlay

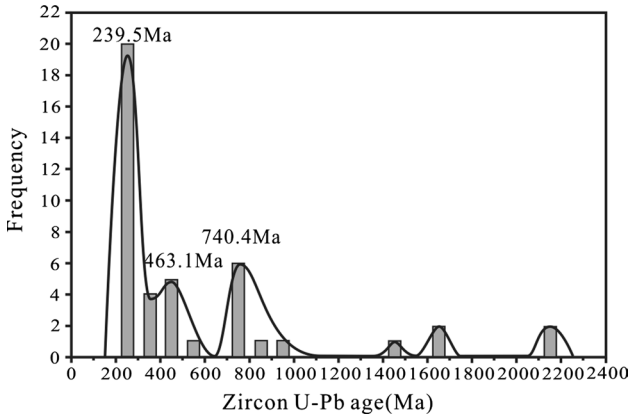

Fig. 6 Age distribution pattern of zircons from Majie muscovite granitoid (sample ALN13178)

1997; Liu et al. 2012b). We suggest that the Ailaoshan block is the northwestern extension of the Nam Co block, and therefore also belongs to the western Yangtze Block (Liu et al. 2012b; Roger et al. 2014).

Generation of the Yinjie and Majie granitoids, and formation of the Ailaoshan rift

The Triassic zircon rims from the Majie and Yuanjiang granitoids possess negative $\varepsilon_{Hf}(t)$ values of −20.4 to −5.3 and −15.3 to −9.0, respectively, whereas the $\varepsilon_{Hf}(t)$ values of inherited zircon cores are more heterogeneous. Similar results have been reported for syn-collisional S-type granitoids, including the gneiss from southern Diancangshan (ca. 243 Ma, $\varepsilon_{Hf}(t) = -14.9$ to −8.0; Lin et al. 2012), the augen gneiss from the Yuanjiang area (ca. 239 Ma, $\varepsilon_{Hf}(t) = -10.7$ to −2.4; Lin et al. 2012), and the Tongtiange leucogranite (ca. 248 Ma, $\varepsilon_{Hf}(t) = -11.1$ to −3.1; Liu et al. 2015a), suggesting that they originated from the partial melting of ancient crust (Fig. 7). Thus, the zircon cores in the Majie and Yuanjiang granitoids were probably inherited from the partial melting of ancient crust. In contrast, I-type granitoids often have uniformly high positive $\varepsilon_{Hf}(t)$ values, such as the gneiss from southern Diancangshan (ca. 235 Ma, $\varepsilon_{Hf}(t) = 10.2$–13.5; Lin et al. 2012), the Huashiban granite from the central part of the Ailaoshan block (ca. 230 Ma, $\varepsilon_{Hf}(t) = 8.4$–13.1; Liu et al. 2014), and the Yinjie granitoid from the northern Ailaoshan block (ca. 247 Ma, $\varepsilon_{Hf}(t) = 7.8$–12.1). These $\varepsilon_{Hf}(t)$ values suggest a mantle contribution to the generation of the source magmas (Fig. 7).

The widespread Permo–Triassic volcanic and plutonic rocks have been interpreted to reflect the closure of the Ailaoshan Ocean, regardless of whether they occur to the west or east of the Ailaoshan suture zone (e.g., Jian et al. 2009a, b; Fan et al. 2010; Liu et al. 2014, 2015a). There is no doubt that the volcanic and plutonic rocks located to the west of the Ailaoshan suture zone were formed by the westward subduction of the oceanic plate. Geochemically, these magmatic rocks show arc-type characteristics (Jian et al. 2009a; Fan et al. 2010; Liu et al. 2011; Lai et al. 2014a). However, contemporaneous volcanic rocks are recognized to the east of the Ailaoshan suture zone, such as the Early Triassic Maoheshan basalt (Liu et al. 2011; Hu et al. 2015). In addition, as shown in Fig. 2, massive granitoids occur to the east of the Ailaoshan suture zone or even within the Ailaoshan high-grade metamorphic belt (Li et al. 2008; Qi et al. 2010; Lin et al. 2012; Liu et al. 2014, 2015a; Lai et al. 2014b). Therefore, it is questionable whether these magmatic rocks formed in response to the westward subduction of the Ailaoshan oceanic plate beneath the Simao block.

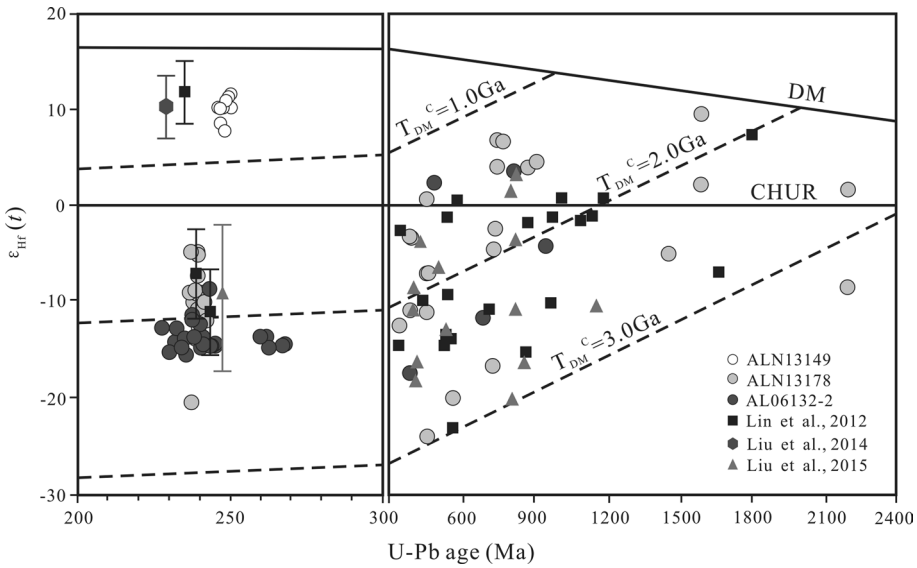

Fig. 7 Zircon Hf isotopic Characteristics of granitoids from the Ailaoshan high-grade metamorphic belt, the $\varepsilon_{Hf}(t)$ value are from Lin et al. (2012), Liu et al. (2014, 2015a) and this study

Late Permian magmatic rocks have been newly identified from distinct geochemical signatures, which were long interpreted to be a Devono–Carboniferous Ailaoshan ophiolite. These include the Pingzhang gabbro (ca. 258 Ma; Lai et al. 2014b) and the Panjiazhai metabasalt (Shen et al. 1998; Mo et al. 1998). These rocks often occur as faulted slices and blocks in the tectonic mélange, which makes it difficult to interpret their initial tectonic setting. Geochemical evidence suggests that late Permian magmatism in the Ailaoshan block occurred in a continental rift setting and has a close geochemical association with coeval continental rift magmatism in the Ganzi–Litang Ocean and the Jinping–Song Da rift (Lai et al. 2014b). The Maoheshan basalt, which has an E-MORB or within-plate-basalt affinity, is thought to have formed in a continent–ocean transition setting during the early stage of the evolution of the Ailaoshan Ocean (Hu et al. 2015). However, based on its Early Triassic age (ca. 249 Ma; Liu et al. 2011), we prefer the interpretation that the Maoheshan basalt is related to the evolution of the Ailaoshan rift.

The Ailaoshan rift probably opened before the late Permian between the Yangtze block and the Ailaoshan microblock, which led to the generation of continental-rift mafic rocks in the Panjiazhai, Pingzhang, and Maoheshan areas. Plutonism to the east of the Ailaoshan suture zone occurred in response to closure of the Ailaoshan rift, which began in the Middle Triassic. The Yinjie granitoid (ca. 247 Ma), which yields positive zircon $\varepsilon_{Hf}(t)$ values, was generated from partial melting of juvenile crust. The pervasive inherited zircon cores and negative $\varepsilon_{Hf}(t)$ values of zircon rims from the Majie (ca. 240 Ma) and Yuanjiang (ca. 238 Ma) granitoids indicate that they originated from the partial melting of ancient crust.

Regionally, it is widely accepted that the Ailaoshan suture zone is linked with the Jingshajiang suture zone to the northwest and the Song Ma suture zone to the southeast (e.g., Zhong 1998; Metcalfe 2006, 2013; Jian et al. 2009a, b). The Ailaoshan block corresponds to the Zhongzan and Nam Co blocks, as discussed above. In addition, the opening of the Ganzi–Litang Ocean (ca. 292 Ma; Yan et al. 2005) was broadly coeval with the opening of the Jinping–Song Da rift during the early Permian (Hanski et al. 2004). Based on the consistent Late Triassic timing of rifting and suturing (Liu et al. 2012a, b; He et al. 2013; Wang et al. 2013b; Peng et al. 2014), the Ganzi–Litang Ocean may be a northwestward extension of the Jinping–Song Da rift (Liu et al. 2012b). Therefore, based on these spatial–temporal relationships, it is reasonable to argue for the existence of an Ailaoshan rift that was both located between, and connected to the Ganzi–Litang Ocean to the northwest and the Jinping–Song Da rift to the southeast.

Implications for the tectonic evolution of the Paleo-Tethyan Ocean

Paleogeographic reconstructions suggest the late Paleozoic to early Mesozoic Paleo-Tethyan

Ocean in Southeast Asia was characterized by an archipelago of arcs or continental ribbons separating multiple seaways (Fig. 8a, b). The Paleo-Tethyan archipelago had a configuration analogous to that of the present-day southwestern Pacific Ocean (Liu et al. 2002; Metcalfe 2006, 2013; Zi et al. 2012a).

Integrated geological, geochronological, and geochemical studies of the Jinshajiang–Ailaoshan–Song Ma suture zone suggest that the ocean, as a subsidiary ocean in the Paleo-Tethyan system, opened in the Silurian and closed in the early Permian (Zhong 1998; Wang et al. 2000; Jian et al. 2008, 2009a, b; Fan et al. 2010; Zi et al. 2012a; Vuong et al. 2013; Lai et al. 2014a, b; Xia et al. 2015). Extensive Permo–Triassic magmatism developed to the west of the Jinshajiang–Ailaoshan–Song Ma suture zone during the westward subduction of the oceanic plate and the subsequent collision between the eastern Qiangtang–Simao–Indochina and Yangtze blocks (Hoa et al. 2008; Jian et al. 2008, 2009b; Fan et al. 2010; Liu et al. 2011, 2012b, 2015a; Zi et al. 2012a, b, c; Lai et al. 2014a; Roger et al. 2014; Shi et al. 2015). However, Reid et al. (2005) and Lepvrier et al. (2004) argued that subduction zones along the Jinshajiang and Song Ma sutures were east-dipping and resulted in extension within the Ganzi–Litang Ocean and the Jinping–Song Da rift. Roger et al. (2008, 2010) even suggested that the Jinshajiang orogenic belt was active with divergent double subduction from the late Permian to the Early Triassic. Furthermore, the widespread Permo–Triassic granitoids and mafic volcanic rocks to the east of the Ailaoshan suture zone require an alternative interpretation.

The following tectonic model is proposed for the early Permian to Late Triassic tectono-magmatic evolution of the Ailaoshan tectonic belt, and to interpret the relationship between the spatial–temporal evolutions of the Jinshajiang–Ailaoshan–Song Ma Ocean and the Ganzi–Litang–Ailaoshan–Jinping–Song Da ocean/rift.

The Precambrian crystalline basement and Paleozoic metamorphic rocks in the Zhongzan–Ailaoshan–Nam Co block are lithologically similar to those of the western Yangtze block. Their correlation may reveal a pre-Mesozoic link between the two blocks. The existence of late Permian extension-related magmatism in the Ganzi–Litang suture zone and the Ailaoshan–Jinping–Song Da rift suggests that opening and spreading of the Ganzi–Litang–Ailaoshan–Jinping–Song Da ocean/rift was preceded by intracontinental extension and rifting along the western margin of the Yangtze block, probably during the early

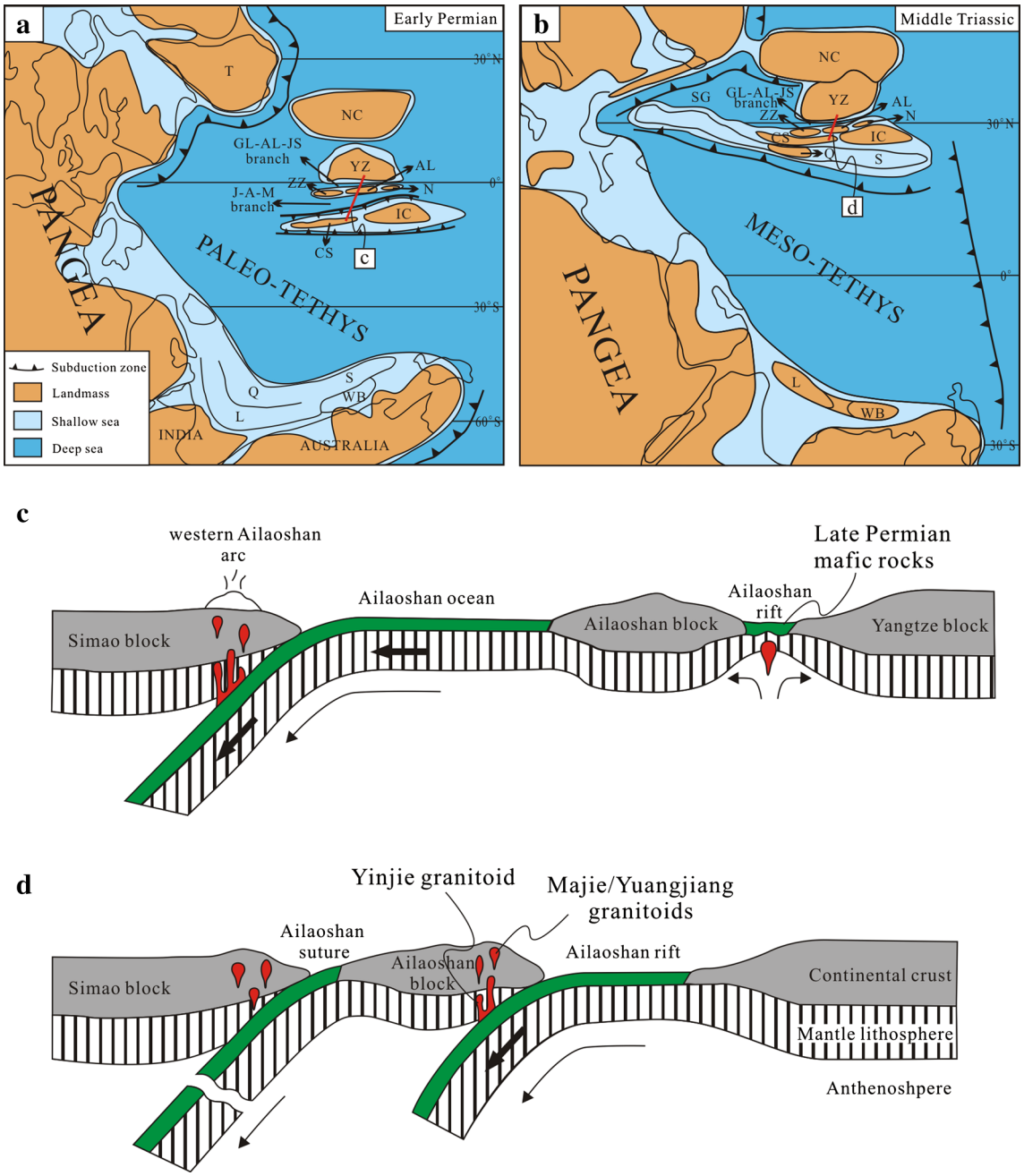

Fig. 8 Paleogeographic reconstructions of the eastern Tethyan region in **a** early Permian and **b** Middle Triassic (modified after Metcalfe 2006; Zi et al. 2012a). *NC* North China, *YZ* Yangtze, *T* Tarim, *IC* Indochina, *CS* Changdu-Simao, *Q* Qiangtang, *S* Sibumasu, *L* Lhasa, *WB* West Burma, *ZZ* Zhongzan, *AL* Ailaoshan, *N* Nam Co, *J–A–M* Jinshajiang–Ailaoshan–Song Ma ocean, *GL–AL–JS* Ganzi–Litang ocean–Ailaoshan rift–Jinping–Song Da rift; **c** Subduction of the Ailaoshan oceanic lithosphere facilitated the separation of the Ailaoshan micro-block from the western Yangtze block through opening the Ailaoshan rift since the early Permian; **d** formation of the Yinjie (ca. 247 Ma), Majie (ca. 240 Ma) and Yuanjiang (ca. 238 Ma) granitoids indicate the closure of the Ailaoshan rift. Positions of transects are marked as *red line* in **a**, **b**

Permian (Fig. 8a, c). Extensive granitoid magmatism to the east of the Ailaoshan suture is likely attributed to partial melting of ancient and juvenile crusts during closure of the Ailaoshan rift since the Early Triassic (Fig. 8b, d). The corresponding magmatism developed more broadly along the Ganzi–Litang suture zone and the Jinping–Song Da rift.

Slab-pull force, originating from gravitational drag by the subducting oceanic slab, was probably an important factor contributing to the successive rifting, separation,

and northward translation of blocks from the northeastern margin of the Gondwana continent during the evolution of the Paleo-Tethyan Ocean, as well as from the western Yangtze margin (Zhong 1998). Progressive thermal thinning of lithosphere by an upwelling asthenosphere may have ultimately led to the rifted western Yangtze margin and resultant sea-floor spreading events (Jian et al. 2009b). Subduction of the Jinshajiang–Ailaoshan–Song Ma oceanic lithosphere likely facilitated the separation of a microcontinental slab (i.e., the Zhongzan–Ailaoshan–Song Ma micro-block) from the thinned and weak passive continental margin of the western Yangtze block. This probably occurred through the opening of the Ganzi–Litang–Ailaoshan–Jinping–Song Da ocean/rift, beginning in the early Permian, which may represent a small, subsidiary Paleo-Tethyan Ocean beyond the western Yangtze block. The spatial–temporal coupling of the tectonic evolution of these segments provides further evidence for this scenario.

Following the collision between the Indian and Eurasian plates in the Tertiary, over 500 km of left-lateral movement along the ASRR shear zone has strongly deformed and displaced many geological units that were once continuous (Tapponnier et al. 1982, 1990; Leloup et al. 1995; Chung et al. 1997). The intense shearing not only occurred within the high-grade metamorphic belt, but also affected the low-grade metamorphic belt. Oligocene metamorphic overprints are obvious in some of the Middle Triassic granitoids, such as the Heping granite (Lai et al. 2014b) and the augen gneiss in the Yuanjiang area (Lin et al. 2012).

The tectonic units in this region that have undergone intense shearing are characterized by long and narrow shapes that make them difficult to distinguish from each other. Additional work is required to test our new model, particularly as it pertains to the interpretation of volcanic and sedimentary rocks and their relationship to the evolution of the Ailaoshan rift.

Conclusions

1. The Yinjie, Majie, and Yuanjiang granitoids from the Ailaoshan high-grade metamorphic belt were emplaced at ca. 247, ca. 240, and ca. 238 Ma, respectively. The uniformly positive zircon $\varepsilon_{Hf}(t)$ values of the Yinjie granitoid (7.8–12.1) indicate the derivation of its source magma from partial melting of juvenile continental lower crust, whereas the negative zircon $\varepsilon_{Hf}(t)$ values of the Majie and Yuanjiang granitoids (−20.4 to −5.3 and −15.3 to −9.0, respectively) indicate the source magmas originated from partial melting of ancient crust.
2. The inherited and detrital zircon age spectra, and their zircon Hf model ages, indicate the occurrence of complex source rocks along the Ailaoshan micro-block and are comparable to those of the western Yangtze block. The Ailaoshan, Zhongzan, and Nam Co micro-blocks are suggested to have been derived from the western margin of the Yangtze block.
3. The westward subduction of the Jinshajiang–Ailaoshan–Song Ma oceanic lithosphere triggered rifting along the passive continental margin of the western Yangtze block and therefore led to the development of the Ganzi–Litang Ocean, an Ailaoshan rift, and the Jinping–Song Da rift. The closure of the Ailaoshan rift during the Early to Middle Triassic can reasonably explain the Triassic magmatism to the east of the Ailaoshan suture zone, including the Yinjie, Majie, and Yuanjiang granitoids.

Acknowledgments This study is funded by National Natural Science Foundation of China (41430211), the National Key Basic Research and Development Project (2015CB452600), and China Geological Survey (1212011120343).

References

BGMRYP (Bureau of Geology and Mineral Resources of Yunnan Province) (1990) Regional Geology of Yunnan Province, Geology Publishing House, Beijing (**in Chinese with English abstract**)

Blichert-Toft J, Albarede F (1997) The Lu–Hf isotope geochemistry of chondrites and evolution of mantle-crust system. Earth Planetary Sci Lett 148:243–258

Cai YF, Wang YJ, Cawood PA, Fan WM, Liu HC, Xing XW, Zhang YZ (2014) Neoproterozoic subduction along the Ailaoshan zone, South China: Geochronological and geochemical evidence from amphibolite. Precambriam Res 245:13–28

Cao SY, Liu JL, Leiss B, Neubauer F, Genser J, Zhao CQ (2011a) Oligo-Miocene shearing along the Ailao Shan-Red River shear zone: constraints from structural analysis and zircon U/Pb geochronology of magmatic rocks in the Diancang Shan massif, SE Tibet, China. Gondwana Res 19:975–993

Cao SY, Neubauer F, Liu JL, Genser J, Leiss B (2011b) Exhumation of the Diancang Shan metamorphic complex along the Ailao Shan-Red River belt, southwestern Yunnan, China: evidence from 40Ar/39Ar thermochronology. J Asian Earth Sci 42:525–550

Chang C (1997) Geology and tectonics of Qinghai-Xizang Plateau. Solid Earth Sciences Research in China. Science Press, Beijing, pp 153 (**in Chinese**)

Chung SL, Lee TY, Lo CH, Wang PL, Chen CY, Yem NT, Hoa TT, Wu GY (1997) Intraplate extension prior to continental extrusion along the Ailao Shan-Red River shear zone. Geology 25:311–314

Deng J, Wang QF, Li GJ, Li CS, Wang CM (2014) Tethys tectonic evolution and its bearing on the distribution of important mineral deposits in the Sanjiang region, SW China. Gondwana Res 26:419–437

Fan WM, Wang YJ, Zhang AM, Zhang FF, Zhang YZ (2010) Permian arc-back-arc basin development along the Ailaoshan tectonic zone: geochemical, isotopic and geochronological evidence from the Mojiang volcanic rocks, Southwest China. Lithos 119:553–568

Findlay RH (1997) The Song Ma Anticlinorium, northern Vietnam: the structure of an allochthonous terrane containing an early Paleozoic island arc sequence. J Asian Earth Sci 15:453–464

Greentree MR, Li ZX (2008) The oldest known rocks in south-western China: SHRIMP U-Pb magmatic crystallisation age and detrital provenance analysis of the Paleoproterozoic Dahongshan Group. J Asian Earth Sci 33:289–302

Griffin WL, Pearson NJ, Belousova E, Jackson SE, Van Achterbergh E, O'Reilly SY, Shee SR (2000) The Hf isotope composition of cratonic mantle: LAM-MC-ICPMS analysis of zircon megacrysts in kimberlites. Geochim Cosmochim Acta 64:133–147

Griffin WL, Wang X, Jackson SE, Pearson NJ, Oreilly SY, Xu XS, Zhou XM (2002) Zircon chemistry and magma mixing, SE China: in situ analysis of Hf isotopes, Tonglu and Pingtan igneous complexes. Lithos 61:237–269

Hanski E, Walker RJ, Huhma H, Polyakov GV, Balykin PA, Hoa TT, Phuong NT (2004) Origin of Permian-Triassic komatiites, northwestern Vietnam. Contrib Miner Petrol 147:453–469

He DF, Zhu WG, Zhong H, Ren T, Bai ZJ, Fan HP (2013) Zircon U-Pb geochronology and elemental and Sr–Nd–Hf isotopic geochemistry of the Daocheng granitic pluton from the Yidun Arc, SW China. J Asian Earth Sci 67–68:1–17

Hoa TT, Anh TT, Phuong NT, Dung PT, Anh TV, Izokh AE, Borisenko AS, Lan CY, Chung SL, Lo CH (2008) Permo-Triassic intermediate-felsic magmatism of the Truong Son belt, eastern margin of Indochina. C R Geosci 340:112–126

Hou KJ, Li YH, Zou TR, Qu XM, Shi YR, Xie GQ (2007) Laser ablation-MC-ICP-MS technique for Hf isotope microanalysis of zircon and its geological applications. Acta Petrol Sin 23:2595–2604

Hou KJ, Li YH, Tian YY (2009) In situ U-Pb zircon dating using laser ablation-multi ion counting-ICP-MS. Miner Deposits 28:481–492 **(in Chinese with English abstract)**

Hu WJ, Zhong H, Zhu WG, He XH (2015) Elemental and Sr–Nd isotopic geochemistry of the basalts and microgabbros in the Shuanggou ophiolite, SW China: implication for the evolution of the Palaeotethys Ocean. Geol Mag 152:210–224

Jian P, Liu DY, Sun XM (2008) SHRIMP dating of the Permo-Carboniferous Jinshajiang ophiolite, southwest China: geochronological constraints for the evolution of Paleo-Tethys. J Asian Earth Sci 32:371–384

Jian P, Liu DY, Kroner A, Zhang Q, Wang YZ, Sun XM, Zhang W (2009a) Devonian to Permian plate tectonic cycle of the Paleo-Tethys orogen in southwest China (I): geochemistry of ophiolites, arc/back-arc assemblages and within-plate igneous rocks. Lithos 113:748–766

Jian P, Liu DY, Kroner A, Zhang Q, Wang YZ, Sun XM, Zhang W (2009b) Devonian to Permian plate tectonic cycle of the Paleo-Tethys Orogen in southwest China (II): insights from zircon ages of ophiolites, arc/back-arc assemblages and within-plate igneous rocks and generation of the Emeishan CFB province. Lithos 113:767–784

Jian P, Wang XF, He LQ, Wang CS (1998) U-Pb Zircon Dating of the Shuanggou Ophiolite from Xingping County, Yunnan Province. Acta Petrol Sin 14:207–211 **(in Chinese with English abstract)**

Lai CK, Meffre S, Crawford AJ, Zaw K, Xue CD, Halpin JA (2014a) The Western Ailaoshan Volcanic Belts and their SE Asia connection: a new tectonic model for the Eastern Indochina Block. Gondwana Res 26:52–74

Lai CK, Meffre S, Crawford AJ, Zaw K, Halpin JA, Xue CD, Salam A (2014b) The Central Ailaoshan ophiolite and modern analogs. Gondwana Res 26:75–88

Leloup PH, Harrison TM, Ryerson FJ, Chen WJ, Li Q, Tapponnier P, Lacassin R (1993) Structural, petrological and thermal evolution of a Tertiary Ductile strike-slip shear zone, Diancang Shan, Yunnan. J Geophys Res 98:6715–6743

Leloup PH, Lacassin R, Tapponnier P, Scharer U, Zhong DL, Liu XH, Zhang LS, Ji SC, Trinh PT (1995) The Ailao Shan-Red River shear zone (Yunnan, China), Tertiary transform boundary of Indochina. Tectonophysics 251:3–84

Leng CB, Huang QY, Zhang XC, Wang SX, Zhong H, Hu RZ, Bi XW, Zhu JJ, Wang XS (2014) Petrogenesis of the Late Triassic volcanic rocks in the Southern Yidun arc, SW China: constraints from the geochronology, geochemistry, and Sr–Nd–Pb–Hf isotopes. Lithos 190–191:63–382

Lepvrier C, Maluski H, Tich VV, Leyreloup A, Thi PT, Vuong NV (2004) The Early Triassic Indosinian orogeny in Vietnam (Truong Son Belt and Kontum Massif): implications for the geodynamic evolution of Indochina. Tectonophysics 393:7–118

Li ZX, Li XH, Kinny PD, Wang J, Zhang S, Zhou H (2003) Geochronology of Neoproterozoic syn-rift magmatism in the Yangtze Craton, South China and correlations with other continents: evidence for a mantle superplume that broke up Rodinia. Precambrian Res 122:5–109

Li BL, Ji JQ, Fu XY, Gong JF, Song B, Qing JC, Zang C (2008) Zircon SHRIMP dating and its geological implications of the metamorphic rocks in Ailao Shan-Diancang Mountain Ranges, western Yunnan. Acta Petrol Sin 24:322–2330 **(in Chinese with English abstract)**

Lin TH, Chung SL, Chiu HY, Wu FY, Yeh MW, Searle MP, Iizuka Y (2012) Zircon U–Pb and Hf isotope constraints from the Ailao Shan-Red River shear zone on the tectonic and crustal evolution of southwestern China. Chem Geol 291:3–37

Liu BP, Feng QL, Chonglakmani C, Helmcke D (2002) Framework of Paleotethyan archipelago ocean of western Yunnan and its elongation towards north and south. Earth Sci Front 9:61–171 **(in Chinese with English abstract)**

Liu JL, Wang AJ, Cao SY, Zou YX, Tang Y, Chen Y (2008a) Geochronology and tectonic implication of migmatites from Diancangshan, Western Yunnan, China. Acta Petrol Sin 24:413–420 **(in Chinese with English abstract)**

Liu YS, Hu ZC, Gao S, Gunther D, Xu J, Gao CG, Chen HH (2008b) In situ analysis of major and trace elements of anhydrous minerals by LA–ICP–MS without applying an internal standard. Chem Geol 257:34–43

Liu YS, Hu ZC, Zong KQ, Gao CG, Gao S, Xu J, Chen HH (2010) Reappraisement and refinement of zircon U–Pb isotope and trace element analyses by LA–ICP–MS. Chin Sci Bull 55:1535–1546

Liu C, Deng JF, Liu JL, Shi YL (2011) Characteristics of volcanic rocks from Late Permian to Early Triassic in Ailaoshan tectonomagmatic belt and implications for tectonic settings. Acta Petrol Sin 27:590–3602 **(in Chinese with English abstract)**

Liu JL, Tang Y, Tran MD, Cao SY, Zhao L, Zhang ZC, Zhao ZD, Chen W (2012a) The nature of the Ailao Shan-Red River (ASRR) shear zone: constraints from structural, microstructural and fabric analyses of metamorphic rocks from the Diancang Shan, Ailao Shan and Day Nui Con Voi massifs. J Asian Earth Sci 47:231–251

Liu JL, Tran MD, Tang Y, Nguyen QL, Tran TH, Wu WB, Chen JF, Zhang ZC, Zhao ZD (2012b) Permo-Triassic granitoids in the northern part of the Truong Son belt, NW Vietnam: geochronology, geochemistry and tectonic implications. Gondwana Res 22:628–644

Liu HC, Wang YJ, FanWM Zi JW, Cai YF, Xing XW (2014) Petrogenesis and tectonic implications of Late-Triassic high $\varepsilon Nd(t)$-$\varepsilon Hf(t)$ granites in the Ailaoshan tectonic zone (SW China). Sci China-Earth Sci 57:181–2194

Liu HC, Wang YJ, Cawood PA, Fan WM, Cai YF, Xing XW (2015a) Record of Tethyan ocean closure and Indosinian collision along the Ailaoshan suture zone (SW China). Gondwana Res 27:1292–1306

Liu JL, Chen XY, Wu WB, Tang Y, Tran MD, Nguyen QL, Zhang ZC, Zhao ZD (2015b) New tectono-geochronological constraints on timing of shearing along the Ailao Shan-Red River shear zone: implications for genesis of Ailao Shan gold mineralization. J Asian Earth Sci 47:231–251

Metcalfe I (2006) Paleozoic and Mesozoic tectonic evolution and palaeogeography of East Asian crustal fragments: The Korean Peninsula in context. Gondwana Res 9:24–46

Metcalfe I (2013) Gondwana dispersion and Asian accretion: tectonic and palaeogeographic evolution of eastern Tethys. J Asian Earth Sci 66:1–33

Mo XX, Shen SY, Zhu QW (1998) Volcanics-ophiolite and Mineralization of Middle-Southern Part in Sanjiang Area of Southwestern China. The Geological Publishing House, Beijing **(in Chinese with English Abstract)**

Peng TP, Zhao GC, Fan WM, Peng BX, Mao YS (2014) Zircon geochronology and Hf isotopes of Mesozoic intrusive rocks from the Yidun terrane, Eastern Tibetan Plateau: petrogenesis and their bearings with Cu mineralization. J Asian Earth Sci 80:18–33

Qi XX, Zhu LH, Li QH, Hu ZC, Li ZQ (2010) Zircon LA–ICP–MS U–Pb Dating for Mylonitized Granite from the Ailaoshan-Jinshajiang Tectonic Zone in the Eastern Qinghai-Tibet Plateau and Its Tectonic Significance. Acta Geol Sin 84:357–369 **(in Chinese with English abstract)**

Qi XX, Zeng LS, Zhu LH, Hu ZC, Hou KJ (2012) Zircon U–Pb and Lu–Hf isotopic systematics of the Daping plutonic rocks: implications for the Neoproterozoic tectonic evolution of the northeastern margin of the Indochina block, Southwest China. Gondwana Res 21:180–193

Reid AJ, Wilson CJL, Liu S (2005) Structural evidence for the Permo-Triassic tectonic evolution of the Yidun Arc, eastern Tibetan Plateau. J Struct Geol 27:119–137

Reid A, Wilson CJL, Shun L, Pearson N, Belousova E (2007) Mesozoic plutons of the Yidun Arc, SW China: U/Pb geochronology and Hf isotopic signature. Ore Geol Rev 31:88–106

Roger F, Jolivet M, Malavieille J (2008) Tectonic evolution of the Triassic fold belts of Tibet. Comptes Rendus Geosci 340(2–3):180–189

Roger F, Jolivet M, Malavieille J (2010) The tectonic evolution of the Songpan-Garze (North Tibet) and adjacent areas from proterozoic to present: a synthesis. J Asian Earth Sci 39:254–269

Roger F, Jolivet M, Maluski H, Respaut J-P, Munch P, Paquette JL, Van TV, Van VN (2014) Emplacement and cooling of the Dien Bien Phu granitic complex: implications for the tectonic evolution of the Dien Bien Phu Fault (Truong Son Belt, NW Vietnam). Gondwana Res 26:785–801

Searle MP (2006) Role of the Red River Shear Zone, Yunnan and Vietnam, in the continental extrusion of SE Asia. J Geol Soc Lond 163:1025–1036

Searle MP, Yeh MW, Lin TH, Chung SL (2010) Structural constraints on the timing of left-lateral shear along the Red River shear zone in the Ailao Shan and Diancang Shan Ranges, Yunnan, SW China. Geosphere 6:316–338

Shen SY, Wei QR, Cheng HL, Mo XX (1998) Tectonomagmatic types of volcanic rocks in Ailaoshan-Lixianjiang Belt, Nu River-Lancang River–Jinsha River area in China. J Miner and Petrol 18:18–24 **(in Chinese with English abstract)**

Shi MF, Lin FC, Fan WY, Deng Q, Cong F, Tran MD, Zhu HP, Wang H (2015) Zircon U-Pb ages and geochemistry of granitoids in the Truong Son terrane, Vietnam: tectonic and metallogenic implications. J Asian Earth Sci 101:101–120

Sun WH, Zhou MF, Yan DP, Li JW, Ma YX (2008) Provenance and tectonic setting of the Neoproterozoic Yanbian Group, western Yangtze Block (SW China). Precambrian Res 167:213–236

Sun WH, Zhou MF, Gao JF, Yang YH, Zhao XF, Zhao JH (2009) Detrital zircon U–Pb geochronological and Lu–Hf isotopic constraints on the Precambrian magmatic and crustal evolution of the western Yangtze Block, SW China. Precambrian Res 172:99–126

Tang Y, Liu JL, Tran MD, Song ZJ, Wu WB, Zhang ZC, Zhao ZD, Chen W (2013) Timing of left-lateral shearing along the Ailao Shan-Red River shear zone, Western Yunnan: constraints from zircon U–Pb ages from leucocratic dykes in the shear zone along the Ailao Shan Range. Int J Earth Sci 102:605–626

Tapponnier P, Peltzer G, Armijo R, Cobbold P (1982) Propagating extrusion tectonic in Asia: new insights from simple experiments with plasticine. Geology 10:611–616

Tapponnier P, Lacassin R, Leloup PH, Scharer U, Zhong DL, Wu HW, Liu XH, Ji SC, Zhang LS, Zhong JY (1990) The Ailao Shan/Red River metamorphic complex: tertiary leftlateral shear between Indochina and South China. Nature 343:431–437

Trouw RAJ, Passchier CW, Wiersma D (2010) Atlas of mylonites and related microstructures. Springer, Berlin

Vuong NV, Hansen BT, Wemmer K, Lepvrier C, Tich VV, Thang TT (2013) U/Pb and Sm/Nd dating on ophiolitic rocks of the Song Ma suture zone (northern Vietnam): evidence for upper paleozoic paleotethyan lithospheric remnants. J Geodynamics 69:140–147

Wang XF, Metcalfe I, Jian P, He LQ, Wang CS (2000) The Jinshajiang-Ailaoshan Suture Zone, China: tectonostratigraphy, age and evolution. J Asian Earth Sci 18:675–690

Wang BQ, Wang W, Chen WT, Gao JF, Zhao XF, Yan DP, Zhou MF (2013a) Constraints of detrital zircon U–Pb ages and Hf isotopes on the provenance of the Triassic Yidun Group and tectonic evolution of the Yidun Terrane, Eastern Tibet. Sed Geol 289:74–98

Wang BQ, Zhou MF, Chen JF, Gao JF, Yan DP (2013b) Petrogenesis and tectonic implications of the Triassic volcanic rocks in the northern Yidun Terrane, Eastern Tibet. Lithos 175–176:285–301

Wang DB, Tang Y, Liao SY, Yin GF, Sun ZM, Wang LQ, Wang BD (2013c) Zircon U-Pb dating and its geological implications of the metamorphic rock series in Ailao Shan Ranges, western Yunnan. Acta Petrol Sin 29:1261–1278 **(in Chinese with English abstract)**

Wang QF, Deng J, Li C, Li GJ, Yu L, Qiao L (2014) The boundary between the Simao and Yangtze blocks and their locations in Gondwana and Rodinia: constraints from detrital and inherited zircons. Gondwana Res 26:438–448

Wu FY, Yang YH, Xie LW, Yang JH, Xu P (2006) Hf isotopic compositions of the standard zircons and baddeleyites used in U-Pb geochronology. Chem Geol 234:105–126

Xia XP, Nie XS, Lai CK, Wang YJ, Long XP, Meffre S (2015) Where was the Ailaoshan Ocean and when did it open: a perspective based on detrital zircon U–Pb age and Hf isotope evidence. Gondwana Res. doi:10.1016/j.gr.2015.08.006

Xie LW, Zhang YB, Zhang HH, Sun JF, Wu FY (2008) In situ simultaneous determination of trace elements, U–Pb and Lu–Hf isotopes in zircon and baddeleyite. Chin Sci Bull 53:1565–1573

Yan DP, Zhou MF, Song HL, Wang XW, Malpas J (2003) Origin and tectonic significance of a Mesozoic multi-layer over-thrust system within the Yangtze Block (South China). Tectonophysics 361:254–293

Yan QR, Wang ZQ, Liu SW (2005) Opening of the Tethys in southwest China and its significance to the breakup of East Gondwanaland in late Paleozoic: evidence from SHRIMP U–Pb zircon analyses for the Garzê ophiolite block. Chin Sci Bull 50:256–264

Yumul GP, Zhou MF, Wang CY, Zhao TP, Dimalanta CB (2008) Geology and geochemistry of the Shuanggou ophiolite (Ailao Shan ophiolitic belt), Yunnan Province, SW China: evidence for a slow-spreading oceanic basin origin. J Asian Earth Sci 32:385–395

Zhai MG, Cong BL, Qiao GS, Zhang RY (1990) Sm–Nd and Rb–Sr geochronology of metamorphic rocks from SW Yunnan orogenic zones, China. Acta Petrol Sin 4:1–11 **(in Chinese with English abstract)**

Zhao GC, Cawood PA (2012) Precambriam geology of China. Precambrian Res 222–223:13–54

Zhao JH, Zhou MF, Yan DP, Yang YH, Sun M (2008) Zircon Lu–Hf isotopic constraints on Neoproterozoic subduction-related crustal growth along the western margin of the Yangtze Block, South China. Precambrian Res 163:189–209

Zhao XF, Zhou MF, Li JW, Sun M, Gao JF, Sun WH, Yang JH (2010) Late Paleoproterozoic to early Mesoproterozoic Dongchuan Group in Yunnan, SW China: implications for tectonic evolution of the Yangtze Block. Precambrian Res 182:57–69

Zhong DL (1998) The Paleo-Tethyan Orogenic Belts, Western Yunnan and Sichuan Provinces (in Chinese). Science Press, Beijing

Zhou MF, Yan DP, Kennedy AK, Li YQ, Ding J (2002) SHRIMP U–Pb zircon geochronological and geochemical evidence for Neoproterozoic arc-magmatism along the western margin of the Yangtze Block, South China. Earth Planet Sci Lett 196:51–67

Zhu JJ, Hu RZ, Bi XW, Zhong H, Chen H (2011) Zircon U–Pb ages, Hf–O isotopes and whole-rock Sr–Nd–Pb isotopic geochemistry of granitoids in the Jinshajiang suture zone, SW China: constraints on petrogenesis and tectonic evolution of the Paleo-Tethys Ocean. Lithos 126:248–264

Zi JW, Cawood PA, Fan WM, Wang YJ, Tohver E (2012a) Contrasting rift and subduction-related plagiogranites in the Jinshajiang ophiolitic melange, southwest China, and implications for the Paleo-Tethys. Tectonics 31:1–18

Zi JW, Cawood PA, Fan WM, Tohver E, Wang YJ, McCuaig TC (2012b) Generation of Early Indosinian enriched mantle-derived granitoid pluton in the Sanjiang Orogen (SW China) in response to closure of the Paleo-Tethys. Lithos 140:166–182

Zi JW, Cawood PA, Fan WM, Wang YJ, Tohver E, McCuaig TC, Peng TP (2012c) Triassic collision in the Paleo-Tethys Ocean constrained by volcanic activity in SW China. Lithos 144:145–160

Zi JW, Cawood PA, Fan WM, Tohver E, Wang YJ, McCuaig TC, Peng TP (2013) Late Permian-Triassic magmatic evolution in the Jinshajiang orogenic belt, SW China and implications for orogenic processes following closure of the Paleo-Tethys. Am J Sci 313:81–112